Precipitation of dolomite from seawater on a Carnian coastal plain (Dolomites, northern Italy): evidence from carbonate petrography and Sr isotopes

Maximilian Rieder[1], Wencke Wegner[2], Monika Horschinegg[2], Stefanie Klackl[1], Nereo Preto[3], Anna Breda[3], Susanne Gier[1], Urs Klötzli[2], Stefano M. Bernasconi[4], Gernot Arp[5], Patrick Meister[1]

[1] Department of Geodynamics and Sedimentology, University of Vienna, Althanstr. 14, 1090 Vienna, Austria

[2] Department of Lithospheric Research, University of Vienna, Althanstr. 14, 1090 Vienna, Austria

[3] Department of Geosciences, University of Padova, Via Gradenigo 6, 35131 Padova, Italy

[4] Geological Institute, ETH Zürich, Sonneggstr. 5, 8092 Zürich, Switzerland

[5] Geoscience Centre, University of Göttingen, Goldschmidtstr. 3, 37077 Göttingen, Germany

Correspondence to: Patrick Meister (patrick.meister@univie.ac.at)

Abstract. The geochemical conditions conducive to dolomite formation in shallow evaporitic environments along the Triassic Tethyan margin are still poorly understood. Large parts of the Triassic dolomites in the Austroalpine and the Southern Alpine realm are affected by late diagenetic or hydrothermal overprinting, but recent studies from the Carnian Travenanzes Formation (Southern Alps) provide evidence of primary dolomite. Here a petrographic and geochemical study of dolomites intercalated in a 100-m-thick Carnian sequence of distal alluvial plain deposits is presented to gain better insight into the conditions and processes of dolomite formation. The dolomites occur as 10- to 50-cm-thick homogenous beds, mm-scale laminated beds, and nodules associated with palaeosols. The dolomite is nearly stoichiometric with slightly attenuated ordering reflections. Sedimentary structures indicate that the initial primary dolomite or precursor phase consisted largely of unlithified mud. Strontium isotope ratios ($^{87}Sr/^{86}Sr$) of homogeneous and laminated dolomites reflect Triassic seawater composition, suggesting precipitation in evaporating seawater in a coastal ephemeral lake or sabkha system. However, the setting differed from modern sabkha or coastal ephemeral lake systems by being exposed to seasonally wet conditions with significant siliciclastic input and

the inhibition of significant lateral groundwater flow by impermeable clay deposits. Thus, the ancient Tethyan margin was different from modern analogues of primary dolomite formation.

Keywords Dolomite, Sr isotopes, sabkha, coastal plain, peritidal platform, Travenanzes Formation, ephemeral lake, authigenic carbonate.

1 Introduction

The formation of dolomite [$CaMg(CO_3)_2$] under Earth surface conditions in modern and ancient environments is still a major unsolved problem in sedimentary geology. Dolomite does not precipitate from modern open ocean water, apparently because its nucleation and growth is inhibited by a high kinetic barrier. For the same reason, the precipitation of dolomite under laboratory conditions has also been difficult (cf. Land, 1998), and therefore the factors that may have influenced dolomite formation throughout Earth history also remain poorly constrained. Van Tuyl (1916) discussed several competing theories for dolomite formation, one of which was the chemical theory, whereby dolomite is a primary precipitate, forming as the result of prevailing conditions within the depositional environment. In contrast, stable isotope and fluid inclusion data often indicate that massive dolomites formed due to replacement of precursor calcium carbonate during burial diagenesis, i.e., at higher temperatures and under conditions decoupled from the ancient depositional environment. Chilingar (1965) suggested that the portion of dolomite in carbonates increases with geological age, implying replacement during burial. However, burial dolomitization requires a mechanism to pump large volumes of Mg-rich water through porous rock (Machel, 2004), and is not always a viable process. There is evidence that large amounts of dolomite could have formed under near-surface conditions (penecontemporaneous dolomite) at certain times in Earth's history, and several studies linked the abundance of dolomite to secular variation in

seawater chemistry, with primary dolomite preferentially forming during times of "calcite seas" (Given and Wilkinson, 1987; Warren, 2000; Burns et al., 2000).

In contrast, penecontemporaneous dolomite formation seems to have prevailed in the Tethyan realm during the Triassic (Meister et al., 2013, and references therein; Li et al., 2018), in an "aragonite sea", while elsewhere dolomite was not particularly abundant (cf. Given and Wilkinson, 1987). In Norian shallow water dolomites of the Dolomia Principale, Iannace and Frisia (1994) measured oxygen isotope values as positive as +3.5‰, suggesting formation at Earth surface temperatures, whereas dolomites from overlying Lower Jurassic units typically show oxygen isotope signatures of diagenetic overprint at burial temperature. Frisia et al. (1994) interpreted these dolomites to be an early diagenetic replacement of precursor carbonate. In a recent study, Preto et al. (2015) suggested that the dolomites of the Carnian Travenanzes Formation (Fm.) in the Venetian Alps are primary precipitates, i.e. they precipitated directly from solution in the sedimentary environment and not by the replacement of a precursor phase during burial. This interpretation is based on high-resolution transmission electron microscope (HR-TEM) analysis, which revealed that single micron-scale dolomite crystals consist of grains with incoherent crystallographic orientation at the few-nanometre scale (cf. Meister and Frisia, 2019). The nanocrystal structures were not replaced by any of the dolomite phases described by Frisia and Wenk (1993) in Late Triassic dolomites of the Southern Alps; instead they are similar to dislocation-ridden Mg-rich phases observed in dolomite from modern sabkhas and are interpreted as primary in origin (Frisia and Wenk, 1993). This finding is intriguing, not only because it is consistent with primary dolomite formation proposed by Van Tuyl (1916) and observed in many modern environments (e.g., Sabkha of Abu Dhabi: Illing, 1965; Wenk et al., 1993; unlithified dolomite is also mentioned in Bontognali et al., 2010; and Court et al., 2017; Deep Springs Lake, California: Jones, 1965; Clayton et al., 1968; Meister et al., 2011; Coorong Lakes: Von der Borch, 1976, Rosen et al., 1989, Warren et al., 1990; Brejo do Espinho, Brazil; Sánchez-

Román et al., 2009; Lake Acigöl, Turkey: Balci et al., 2016; Lake Neusiedl, Austria: Neuhuber et al., 2015; Lake Van: McCormack et al., 2018), but it also provides a window into ancient primary dolomite formation pathways. This finding is also consistent with recent experiments by Rodriguez-Blanco et al. (2015), demonstrating a nanocrystalline pathway of dolomite nucleation and growth. Critically, nanometre size nuclei show a different surface energy landscape compared to macroscopic crystals, allowing for potentially lower energy barriers, perhaps modified by organic matter, microbial effects, clay minerals or particular water chemistry, and thus, promoting the spontaneous precipitation of dolomite.

The interpretation of primary dolomite in the Travenanzes Fm. needs further validation by nano- and atomic scale analyses and further petrographic and geochemical investigations to establish the sedimentary and geochemical conditions in the depositional environment, an extended mud plain that occurred along the western Tethys margin during the Carnian. In particular, the origin of ionic solutions conducive to dolomite formation is still unclear. Comparison with modern environments shows that ionic solutions may either be seawater-derived, as shown for the sabkhas along the Persian Gulf coast, where several hydrological mechanisms were discussed (Adams and Rhodes, 1960; Hsü and Siegenthaler, 1969; McKenzie et al., 1980, McKenzie, 1981; see Machel, 2004, for an overview; cf. also Teal et al., 2000), or derived from continental groundwater, as shown for the coastal ephemeral lakes of the Coorong area (Australia; Alderman and Skinner, 1957; Von der Borch et al., 1976, Rosen et al., 1989; Warren et al., 1990). While both types of fluid become concentrated during evaporation and are, perhaps, modified by the precipitation of carbonates and evaporites, it remains unclear which source prevailed during deposition of the Travenanzes Formation.

Dolomites occur in the Travenanzes Fm. as intercalated beds in a 100-m-thick sequence of red and green clay. The environment hence differed from modern analogues (e.g. sabkhas) in that it contained large amounts of clay derived from riverine input and deposited on a distal

106 alluvial plain, implying seasonally wet conditions. This facies association shows, except for
107 the horizons containing marine fossils, striking similarity to the Germanic Keuper, which
108 represents an entirely continental playa lake system, and also exhibits intercalations of
109 primary dolomite in red clay (Reinhardt and Ricken, 2000). The Keuper facies association
110 extended over much larger areas than just the Germanic basin during the Carnian. Although
111 the Travenanzes Fm. is clearly located, palaeogeographically, in the Tethyan depositional
112 region (Breda and Preto, 2011), its facies separation from the Germanic Keuper may not be
113 precisely coincident with palaeogeographic features, such as the Vindelician high zone. We
114 suggest that the composition and origin of ionic solutions conducive to primary dolomite
115 formation, from either continental water or seawater, is also an indication of separation
116 between the two palaeogeographic domains.

117 Here we provide a detailed investigation of dolomites of the Travenanzes Fm. to
118 reconstruct the processes and factors conducive to dolomite formation. We specifically
119 searched for sedimentary structures indicating that the initial authigenic dolomite (or a
120 precursor carbonate phase) was unlithified, as would be expected if it spontaneously
121 precipitated from the shallow water bodies of ephemeral lakes or tidal ponds. Radiogenic Sr-
122 isotope ratios ($^{87}Sr/^{86}Sr$) were measured in the dolomites and compared with the established
123 Triassic seawater Sr-isotope curve (Veizer et al., 1999; McArthur et al., 2012) to determine if
124 ionic solutions conducive to dolomite formation were derived from seawater or from
125 continental runoff. To demonstrate contrasting origin of ionic solutions, Sr-isotope values
126 were compared to values from dolomites from the Germanic Keuper, that are of clear
127 continental origin, and to values in modern dolomites showing marine and/or continental
128 influence. Based on new insights, we discuss possible scenarios of dolomite formation that
129 could have prevailed along the western Tethys margin and in similar evaporative
130 environments.
131

2 Geological setting

The Dolomite mountains (Southern Tyrol and Venetian Alps; Fig. 1a) are well known for their characteristic peaks consisting of Triassic carbonate platform limestones and dolomites. These platforms developed all along the margins of the western Tethys ocean (Stampfli and Borel, 2002), and are separated by deep basins in the middle Triassic, and form an extended coastal plain during the Carnian and Norian. The Adriatic plate was rotated almost 90° counter clockwise as a result of the Alpine Orogeny (Ratschbacher et al., 1991; Handy et al., 2010). As a result, deep-water environments are found to the north today, although they were originally located to the east (Fig. 1a). Triassic paleogeography is largely preserved in the Dolomites in spite of Alpine deformation because the Dolomites form a ca. 60 km wide pop-up structure that is bound by the Periadriatic Line to the north and northwest and the Valsugana Fault to the southeast (Fig. 1a, inset). Therefore, the Dolomites were never buried to a greater depth, and did not experience metamorphic overprinting (Doglioni, 1987). The colour alteration index of conodonts in the Heiligkreuz Fm., which underlies the Travenanzes Fm. in this region is 1, suggesting maximum burial temperatures of less than 50°C, which are confirmed by biomarker data (Dal Corso et al., 2012).

The Travenanzes Fm. lies unconformably above the Heiligkreuz Fm., and is overlain by the Dolomia Principale (Hauptdolomit) along a transgressive boundary (Fig. 1b). Large amounts of siliciclastic material were deposited during the Carnian, presumably as a result of a change in climate and increasingly humid episodes, and led to filling of basins that were more than 100 m deep that existed between the carbonate platforms of the Cassian dolomite (Gattolin et al., 2013; 2015). These basin-filling deposits formed a coastal succession or mixed carbonate-siliciclastic ramp, that includes large clinoforms made up of sandstones and conglomerates (Heiligkreuz Fm.; see Preto and Hinnov, 2003; Gattolin et al., 2013; 2015). The topography was entirely evened out and overlain by the Travenanzes Fm., a ca. 100-m-thick and laterally extensive succession of red and green claystone with intercalated

158 dolomites, evaporites and siliciclastic beds (Fig. 2; Kraus, 1969; Breda and Preto, 2011). The
159 Travenanzes Fm. shows interfingering along a south-north transect between conglomerates
160 and sandstones to the south and carbonate-dominated peritidal to sabkha facies to the north
161 (Breda and Preto, 2011). The upper boundary to the Dolomia Principale is time-transgressive,
162 i.e., it becomes younger from north to south. The Travenanzes Fm. consists of three
163 transgressive-regressive cycles, with the highstand deposits showing identical peritidal
164 carbonate facies as the Dolomia Principale (Breda and Preto, 2011). The boundary with the
165 Dolomia Principale is defined by the last occurrence of siliciclastic material (Gianolla et al.,
166 1998).

167 The depositional environment of the siliciclastic facies of the Travenanzes Fm. has been
168 interpreted as a dryland-river system by Breda and Preto (2011). Such a system occurs in arid
169 environments if rivers drain into a coastal alluvial plain, but do not reach the coast.
170 Evaporation along the way may lead to the formation of playa lakes; on the seaward side of
171 the system extended evaporative areas, i.e. coastal sabkhas, develop. Both types of
172 environment are well known for giving rise to modern dolomite formation (see references
173 above). As the Southern Alps were located in tropical latitudes, a warm arid climate, perhaps
174 influenced by a monsoon effect, developed (Muttoni et al., 2003). Rivers provided large
175 amounts of clay, which were partially oxidized under subaerial conditions, leading to a typical
176 red and green clay succession containing palaeosols. This facies association is widespread
177 throughout the Alpine and Tethyan realm during the Carnian, but similar deposits are strongly
178 deformed by alpine tectonics in most Austroalpine units, forming a characteristic band of
179 rauhwacke, the “Raibl beds” (e.g., Czurda and Nicklas, 1970). In the Travenanzes Fm. the
180 entire sequence maintains its depositional architecture, providing a pristine archive to study
181 the intercalated dolomites.

182 The Carnian and Norian deposits of the Keuper in the endorheic Germanic Basin contain a
183 similar facies association as the Travenanzes Fm., but clearly represent continental playa lake

184 deposits (Reinhardt and Ricken (2000; and references therein). Here we consider dolomites
185 from the Germanic Basin of confirmed continental origin for comparison of Sr-isotope
186 compositions of continental and coastal environments.
187
188 **3 Methods**
189 **3.1 Petrographic and mineralogical analysis**
190 A total of 39 hand specimens were collected from the stratigraphic section at Rifugio
191 Dibona, 5 km west of Cortina d'Ampezzo, Italy (46.532727N/12.067161E; Fig. 1; Breda and
192 Preto, 2011). Additional samples of Triassic dolomites from the Germanic Basin (Weser Fm.
193 and Arnstadt Fm. near Göttingen, Northern Germany) and modern dolomite from the
194 Coorong Lagoon (South Australia) and Deep Springs Lake (California) were also analysed for
195 comparison. Polished thin sections were carbon coated for analysis under the scanning
196 electron microscope (SEM) using a FEI Inspect S-50 SEM (Thermo Fisher Scientific,
197 Bremen, Germany) at the University of Vienna. Element contents were determined semi-
198 quantitatively using an EDX detector (EDAX Ametek, New Jersey, United States) under high
199 vacuum and 12.5 kV beam voltage at a working distance of 10 mm. Differences in
200 mineralogy at the micron scale were mapped in backscatter mode with high contrast.
201 For bulk mineralogical analysis, three dolomite samples were ground to a fine powder with
202 a disk mill. Clay mineralogy was determined on 40 g aliquots that were leached two times for
203 24 h in 250 ml of 25% acetic acid to dissolve all carbonate (Hill and Evans, 1965). The clay
204 mineral separates were washed three times with H_2O and centrifuged. The grain size fraction
205 <2 μm was collected by sedimentation in an Atterberg cylinder after 24 h 33 min. Oriented
206 samples were prepared by pipetting the suspensions (10 mg clay/ml) on glass slides and
207 analysed after air drying. To identify expandable clay minerals, the samples were additionally
208 saturated with ethylene-glycol and heated to 550°C (Moore and Reynolds, 1997). X-ray
209 diffraction analysis of bulk samples and clay mineral separates was performed with a

PANalytical X'Pert Pro diffractometer at the University of Vienna, using CuKα radiation with 40 kV and 40 mA. The samples were scanned from 1.76° to 70° 2ϑ with a step size of 0.0167° and 5 s per step. The X-ray diffraction patterns were interpreted using the Panalytical software "X'Pert High score plus" and Moore and Reynolds (1997) for the clay minerals.

3.2 Carbon and oxygen isotope analysis

Carbon and oxygen isotopes were measured on 28 samples which where micro-drilled from thin section cuttings (see below). The samples were analysed with a Delta V Plus mass spectrometer coupled to a GasBench II (Thermo Fisher Scientific, Bremen, Germany) at ETH Zürich (Zürich, Switzerland), following the procedure described in Breitenbach and Bernasconi (2011). The precision was better than 0.1‰ for both isotopes. The oxygen isotope values were corrected for kinetic fractionation during dissolution of dolomite in anhydrous phosphoric acid at 70°C, using a fractionation factor of 1.009926 (Rosenbaum and Sheppard, 1986).

3.3 Radiogenic Sr-isotope analysis

To ensure that Sr from the pure dolomite phase is extracted, specific areas free of clay minerals were defined by SEM and identified using an Olympus SZ61 microscope equipped with a MicroMill sampling system (Electro Scientific Industries). Eleven samples were drilled over an area of 5-10 mm^2, or along a line in laminated rocks, to a depth of 350 μm. To prevent the powder from being dispersed, the samples were drilled within a drop of MilliQ-H_2O, and the suspension was transferred to a centrifuge tube using a pipette.

A sequential extraction was used to determine the mildest reagent that efficiently extracts the pure dolomite phase without attacking other mineral phases. The extractions were routinely performed in capped 2 ml or 15 ml polypropylene tubes at room temperature on a shaker for 10 min to 24 h. The following leaching reagents (always 2 ml) were used: 1 M

236 NaCl, 3.3 M KCl, 0.1 N acetic acid, 1 N acetic acid and 6 N HCl. Each reaction step was
237 repeated once, and the residues were washed with 2 ml of MilliQ H_2O after each step to
238 remove remains of the previous solvent.

239 Extraction efficiency was tested on bulk samples, clay samples, pure celestine and barite
240 purchased from W. Niemetz (Servitengasse 12, 1090 Vienna, Austria), pure dolomite powder
241 from Alfa Aesar (Thermo Fisher – Kandel – GmbH, Postfach 11 07 65, 76057 Karlsruhe,
242 Germany) and a fragment of a single dolomite crystal were analysed as controls. These
243 samples were crushed to a powder in an agate mortar and pestle. Dolomite, barite, and
244 celestine were mixed in a similar ratio as they occur in the dolomites of the Travenanzes Fm.
245 and run through the entire procedure as a control of extraction efficiency; 14 mg of rock
246 powder was weighed out for isotope analysis. In order to rule out contamination by Sr from
247 clay minerals, pure claystone of the Travenanzes Fm. was extracted separately. To ensure that
248 clay samples do not contain carbonate, clay samples were analysed for total organic and
249 inorganic carbon using a LECO RC-612 multiphase carbon analyser, at the Department of
250 Environmental Geosciences at the University of Vienna, with a temperature ramp of 70°C per
251 min to a maximum temperature of 1000°C.

252 Total element concentrations were measured in leachates of three dolomite specimens
253 previously analysed by XRD, and the two claystones. Five ml of each fraction were used for
254 element concentration analysis (the rest was further processed for Sr-isotope analysis; see
255 below). The solutions were evaporated on a heating plate and the residues were re-dissolved
256 in 5 ml 2.5 N HNO_3. This step was repeated with 5 ml 5% HNO_3. Concentrations were
257 measured with a Perkin Elmer 5300 DV ICP-OES at the Department for Environmental
258 Geosciences (University of Vienna). Detection limits for the different elements in rock
259 (μmol/g) were: Al: 0.185, Ca: 0.025, Fe: 0.090, K: 0.026, Mg: 0.041, Mn: 0.002, Na: 0.004,
260 P: 0.032, Ti: 0.002, Ba: 0.001, Sr: 0.001 and Rb: 0.012. The precision of the measurements

(relative standard deviation; RSD) for Al, Ca, K, Mg, Ti, Ba and Sr was ≤0.9% and for Fe, Mn, Na, Rb, P was ≤6.8%.

For Sr-isotope measurements, Sr was separated from interfering ions (e.g. Fe, K, Rb and Ca) using an ion exchange column packed with BIO RAD AG 50W-X8 resin (200-400 mesh, hydrogen form). Leachates were evaporated, dissolved in 6 N HCl and 2.5 N HCl and loaded onto the column in 2 ml 2.5 N HCl. Next, 51 ml of 2.5 N HCl were run through the column to wash out the interfering ions. Sr was eluted with a further 7 ml 2.5 N HCl and dried after collection. Total procedural blanks for Sr were <1 ng and were taken as negligible (the amounts of strontium in the samples were always higher than 100 ng).

The isotopic composition of Sr was measured with a Triton (Thermo Finnigan) thermal ionisation mass spectrometer at the University of Vienna. Sr fractions were loaded (dissolved in 1 µl H_2O) as chlorides and vaporized from a Re double filament. The double filament configuration was used to accelerate detachment of Sr from the filament. The cup configuration was calibrated such that masses 84, 85 (centre cup), 86, 87 and 88 are detected. The NBS987 Sr-isotope standard (number of replicates = 40) shows a $^{87}Sr/^{86}Sr$ ratio of 0.710272 ±0.000004 during the time of investigation, with the uncertainty of the Sr-isotope ratios quoted as 2σ. Interference with ^{87}Rb was corrected using a $^{87}Rb/^{85}Rb$ ratio of 0.386. Within-run mass fractionation was corrected for $^{86}Sr/^{88}Sr = 0.1194$.

4 Results

4.1 Petrographic description of dolomites

Hard cemented beds and nodules of dolomite are intercalated in a 100-m-thick, clay-rich interval (Fig. 2), above which the facies switches sharply to massive, bedded dolomites similar to those of the overlying Dolomia Principale. Macroscopically, three types of dolomite can be distinguished: homogenously bedded dolomite, laminated dolomite, and nodular dolomite (Fig. 3a-c). The lower and middle part of the clay-rich unit contains mainly

287 homogeneous dolomite beds in red clay. Between 40 and 70 m, several horizons with gypsum
288 nodules occur (Fig. 3d). A 30-cm-thick fluvial conglomerate with dolomite-cemented
289 quartzarenites and pebbles of ripped up micritic carbonate occurs at 75 m (Fig. 3e), above
290 which palaeosols with dm-scale vertical peds, possible root traces showing green reduction
291 haloes, and nodular dolomite (calcic vertisols; cf. Cleveland et al., 2008), are more frequent
292 (e.g., Fig. 3b). Ca. 20-cm-thick tempestite beds with *Megalodon* bivalves, foraminifers, and
293 ostracods occur at 65 and 89 m. A pronounced transition occurs in the uppermost ca. 8 metres
294 of the clay-rich interval (Fig. 2b), where the clay entirely changes from a red to a grey colour
295 (Fig. 2c), and laminated dolomites become dominant, while evaporites and palaeosols are
296 absent. The laminated dolomites (Fig. 3c) and cm- to dm-scale dolomite-clay interlayers show
297 intense slumping and soft sediment deformation and pseudo-teepee structures (Figs. 3f, g). A
298 short summary of petrographic analyses of thin sections of the different types of dolomite
299 including the most important features appears below and is compiled in Table S1.
300
301 *Homogenous dolomites*
302 Homogeneous dolomite beds are usually 10 cm to 50 cm thick, embedded within clays and
303 exhibiting sharp, plane-parallel joints. The beds consist of dolomicrite, which was previously
304 described as aphanotopic dolomite by Breda and Preto (2011), according to the extended
305 nomenclature for dolomite fabrics by Randazzo and Zachos (1983). The sediment is matrix-
306 supported and contains irregular, partially rounded mud clasts (intraclasts) that consist of
307 aphanotopic dolomite. Some of the mud clasts contain smaller and somewhat darker mud
308 clasts or peloids (Fig. 4a, arrow). Soft sediment deformation is often not clearly visible due to
309 the homogeneous structure of the mud, but it can be observed where the mud clasts are
310 deformed within the matrix (Fig. 4b). Some of the homogeneous beds in the lower part of the
311 section show sub-millimetre lamination that is only visible under the microscope, where it
312 consists of alternating layers of light (locally coarser) and dark aphanotopic dolomite.

313 The clay content in the homogeneous beds is generally low. A few beds (e.g. at 33.5 m in
314 the section) consist of silty or sandy dolomite, as reflected in a high abundance of detrital
315 quartz in thin section. Pseudomorphs after gypsum occur in a dolomite bed at 120 m (Fig. 4c,
316 d). Moldic porosity occurs within aphanotopic dolomite layers at 43, 65 and 89 m. These
317 correspond to the tempestite beds observed in outcrop (cf. Breda and Preto, 2011).
318 One dolomite bed, located at 64 m in the section, appears homogeneous at outcrop scale,
319 but consists of oolitic grainstone and lacks both an aphanotopic and a cement matrix (Fig. 4e).
320 Ooids show concentric, micritic layers and are either hollow (where the cores may have been
321 dissolved) or filled with sparite, and are surrounded with an isopachous cement rim.
322
323 *Laminated dolomites*
324 Laminated dolomites occur in the upper part of the clay-rich interval, between 90 and 110
325 m in the section (Fig. 4f-i). In the field, the laminated dolomites show an alternation between
326 light grey dolomite laminae and dark grey to black clay laminae. Some dolomite laminae are
327 bent upward and are reminiscent of pseudo-teepee structures (Fig. 4f); the space within the
328 teepee is sometimes infilled with sparry cement. In addition, the bending of the laminae
329 towards the upward directed cuspids is reminiscent of load structures (dish structures), but
330 they also may represent desiccation cracks. The laminae are frequently ripped apart and
331 fragments of laminae occur reworked as flat pebbles embedded in an aphanotopic dolomite
332 matrix (Fig. 4g). Some laminae show a microsparitic appearance and laminar fenestral
333 porosity. In some laminae a clotted peloidal fabric is observed (e.g in Fig. 4f). Laminae are
334 typically graded, whereby the upper part is darker, indicating an increase in the clay content
335 (Fig. 4h, i). The top of the laminae is often truncated by an erosion surface, and rip-up clasts
336 of the fine mud are embedded in the overlying coarse layer. Some laminated dolomites
337 contain continuous layers with inclusions of celestine crystals in the 100-μm-range, some of
338 them with barite in their centre (Fig. 5a-c). Pyrite also occurs.

339 Under the SEM, laminated dolomites show an anhedral structure in the 1-5 μm range. No
340 difference in mineral structure and grain size is observed between mud clasts and the
341 surrounding, often lighter-coloured matrix. Dolomite crystals at the margins between
342 dolomite and clay interlayers often coalesce into 5-μm-scale, round aggregates consisting of
343 several subhedral crystals with different orientations (Fig. 6a, b; the crystals show orientation
344 contrast under BSE mode). Dolomite crystals are often porous, showing a somewhat
345 disordered appearance, but they are surrounded by syntaxial rims. In most cases, the rims
346 entirely fill the intercrystalline space, forming almost hexagonal compromise boundaries (Fig.
347 6c, d). These rims occur both in homogeneous and laminated dolomites.
348
349 *Nodular dolomites*
350 Nodular dolomites (Fig. 3b) often occur in beds of vertical peds linked to palaeosols, as
351 indicated by horizons of vertical cracks showing green alteration fronts. Single nodules may
352 also sporadically occur embedded within metre-thick beds of red and green clay. Nodules are
353 usually 5 to 10 cm in diameter, consist of aphanitic dolomite or occasionally somewhat
354 coarser microspar, and in cross section show both red and pale grey areas. Most nodules also
355 show a deformed or brecciated internal structure with the interstices between the clasts mostly
356 consisting of matrix and clay cutans.
357
358 *Germanic Keuper dolomites*
359 A sample from the Weser Fm. (middle Lehrberg bed; clay pit Friedland, 12 km south of
360 Göttingen, Northern Germany; Seegis, 1997; Arp et al., 2004) exhibits a brittle structure with
361 high porosity. The material consists mainly of packed ooids with few peloids in a sparitic
362 cement matrix. Under the SEM, subhedral to euhedral dolomite in the 5-μm-range are
363 observed within the ooids (not shown).

364 A sample from the Norian Arnstadt Fm. (formerly termed “Steinmergelkeuper”; middle
365 grey series; locality of Krähenberg, 11 km SSW of Göttingen, Northern Germany; Arp et al.
366 2005) shows mm-scale lamination and cm- to dm-sized laminated clasts, which were
367 interpreted as a stromatolite breccia. The laminae contain abundant agglutinated siliciclastic
368 grains (mainly quartz, subordinate albite) and phosphoritic fish scales. The dolomicrite
369 exhibits a subhedral structure in the ≤5 μm range with a few larger, subhedral grains resulting
370 in a porphyrotopic fabric.
371
372 **4.2 Mineralogy**
373 Bulk dolomite shows a position of the 104 peak at a mean d-value of 2.88816 Å (Fig. 7a).
374 This indicates a Ca content of 50.7%, based on the equation of Lumsden (1979). The
375 structural order is indicated by the ratio of the superlattice-ordering peak at (015) to the (110)
376 ordering peak. The height ratio is 0.44, which is near 0.519 (inset in Fig. 7a), indicated for an
377 ordered dolomite in the Highscore database.
378 Clay mineral analysis (Fig. 7b-d) reveals illite in samples TZ14-1 and TZ14-7 and an R3
379 ordered illite-smectite mixed-layer clay mineral in sample TZ14-9. In the ethylene-glycol-
380 saturated state, the broad shoulder at 11.4 Å contains components of the illite 001 reflection
381 and of the fourth order of a 47 Å superstructure peak whose unit cell consists of three 10 Å
382 illite layers and one 17 Å smectite layer (Moore and Reynolds, 1997). This smectite
383 component is not observed in samples TZ14-1 and TZ14-7.
384
385 **4.3 Carbon and oxygen isotopes**
386 Carbon isotope values range from -3.38 to +4‰ VPDB. Oxygen isotope values are
387 between -0.7 and +0.9‰ VPDB (three outliers show values as low as -1.5‰ VPDB; Fig. 8a;
388 PANGAEA Data Archiving & Publication PDI-20535). A clear distinction occurs between
389 nodular dolomites exhibiting negative $\delta^{13}C$ values and homogeneous dolomites showing

positive values. Laminated dolomites exhibit intermediate values and low variability. The oxygen isotopes show an upward increasing trend (Fig. 8b). The calculated temperature of formation assuming a Triassic seawater composition of -1‰ VSMOW using the fractionation equation of Vasconcelos et al. (2005) results in temperatures between 29 and 39°C; more positive values would result in higher water temperatures.

4.4 Elemental composition of the dolomites

Sequentially extracted samples TZ14-1, TZ14-7, and TZ14-9 (PANGAEA Data Archiving & Publication PDI-20535) show Ca contents between 1.68 and 2.33 mmol/g in the 0.1 N acetic acid fraction and between 2.71 and 2.87 mmol/g in the 1 N acetic acid fraction. Mg contents are between 1.61 and 2.34 mmol/g in the 0.1 N acetic acid fraction and between 2.48 and 2.64 mmol/g in the 1 N acetic acid fraction. Based on these concentrations, the amount of dolomite dissolved is between 30 and 43 wt% of the bulk sample in the 0.1 N acetic acid fraction and between 49 and 52 wt% in the 1 N acetic acid fraction of the sequential extraction. In total, between 84 and 90 wt% of the bulk sample were dissolved during these two extraction steps. If molar concentrations of Ca are plotted vs. Mg, a linear trend with a slope of 0.935 is observed (Fig. 9a), indicating 48.3 mol% $MgCO_3$ in the dolomite phase.

Correlation of Sr contents to other elements did not show clear trends. In particular, Sr content did not correlate with Mg or Ca. Sr correlates with K (Fig. 9b), but at the same time, K is extremely low in all clay mineral leachates. The Sr concentrations in bulk dolomite samples (Fig. 10a-c) are in the range of 0.38 and 1.16 μmol/g in the 0.1 N acetic acid fraction and between 0.57 and 0.79 μmol/g in the 1 N acetic acid fraction (except one extremely high value of 34.91 μmol/g in sample TZ14-9). These contents are much higher than in pure clay mineral samples (Fig. 10d) with 0.047-0.417 μmol/g in the 0.1 N acetic acid fraction and even

lower concentrations (<0.19 μmol/g) in the other fractions. In all samples measured by ICP-OES, rubidium (Rb) concentrations are below the detection limit of 0.012 μmol/g.

4.5 Sr isotopes

$^{87}Sr/^{86}Sr$ evolution during leaching experiments

Results of Sr-isotope measurements are available from Rieder et al. (2019). Results of sequential and non-sequential leaching tests of bulk samples TZ14-1, TZ14-7, and TZ14-9 are shown in Fig. 10a-c. $^{87}Sr/^{86}Sr$ ratios decrease in sample TZ14-1 from 0.708125 ±0.000012 to 0.707666 ±0.000004 with increasing strength of the leaching reagent, while the values remain almost constant in sample TZ14-9. The values of bulk dolomite extracted with 1 N acetic acid are slightly lower than in the fraction extracted with 0.1 N acetic acid; only micro-drilled samples show higher values. However, repeating the 0.1 N acetic acid extraction (for 36 h) after a rather intense first extraction (4h, 12h, 4h) results in extremely high values (0.715417 ±0.000250 in TZ14-1 and 0.7192266 ±0.000455 in TZ14-9; not shown in Fig. 10). Standard deviations are also higher than in the other fractions. Highest $^{87}Sr/^{86}Sr$ ratios of up to 0.730453 ±0.000005 in sample TZ14-7 are reached by extraction with 6 N HCl. These fractions show at the same time the lowest Sr concentrations (see above).

Sequential extractions of the clay samples TZ16-1 und TZ16-19B with the lowest TIC of 0.02 wt% (Fig. 10d; PANGAEA Data Archiving & Publication PDI-20535) show a similar increase in the $^{87}Sr/^{86}Sr$ ratio with the sequential extraction steps from 0.1 N acetic acid to 6 N HCl, reaching similar values as in the HCl-fraction of the dolomites (0.722998 ±0.000018 to 0.733910 ±0.000024).

Repeated extractions of chemically pure reference material (Fig. 10e,f) dissolved in 0.1 N acetic acid show a range of $^{87}Sr/^{86}Sr$ ratios in dolomite between 0.709942 ±0.000011 and 0.710831 ±0.000007. Pure single crystals of dolomite extracted sequentially show the highest value (0.708401 ±0.000040) in the 1 M NaCl fraction. Values in the 0.1 N acetic acid fraction

(0.707735 ±0.000006) and the 1 N acetic acid fraction (0.707666 ±0.000006) are lower by almost 0.001 compared to the NaCl fraction.

In pure barite, $^{87}Sr/^{86}Sr$ ratios decrease by about 0.0013 in the extraction sequence from 0.1 N acetic acid to 6 N HCl. Celestine is highly soluble and was only measured in the 1 M NaCl fraction and once in 0.1 N acetic acid. Extracts of pure celestine show similar values as in the 1 M NaCl fraction of the barite-celestine-dolomite mixture (0.708038 ±0.000003), but the mixture show higher values (0.709501 ±0.000040) in the 0.1 N acetic acid fraction.

$^{87}Sr/^{86}Sr$ ratios in micro-drilled dolomite

Eleven dolomite samples were micro-drilled from areas where dolomite was most pure based on examination by SEM and dissolved in 0.1 N acetic acid. The values of the Travenanzes Fm. are in the range of 0.707672 ±0.000003 to 0.707976 ±0.000004 (Fig. 11). The highest value occurs in a dolomite nodule, while no systematic difference between homogenous and laminated dolomite was observed. Dolomite of the Germanic Keuper samples shows significantly higher $^{87}Sr/^{86}Sr$ ratios of 0.709303 ±0.000006 and 0.709805 ±0.000005, respectively.

$^{87}Sr/^{86}Sr$ ratios of modern dolomites (Deep Springs Lake, Coorong Lakes)

Dolomites of Deep Springs Lake show strongly radiogenic values of 0.713086 ±0.000004 and 0.713207 ±0.000004 (Fig. 12), which are much higher than modern seawater values, with a $^{87}Sr/^{86}Sr$ ratio of 0.709234 ±0.000009 (DePaolo and Ingram, 1985). In contrast, dolomite from the Coorong Lakes (Milne Lake; Fig. 12) exhibits ratios between 0.709251 ±0.000004 and 0.709275 ±0.000003, which is very close to the ratio of modern seawater. Different incubation times (5 min und 10 h) in 0.1 N acetic acid had no influence on the isotope ratios.

5 Discussion

466 **5.1 Interpretation of microfacies within different types of dolomite**

467 *Homogeneous dolomite beds*

468 The homogeneous dolomite beds, which are mainly intercalated in the lower, clay-rich part
469 of the Travenanzes Fm., consist of fine-grained dolomicrite (aphanotopic dolomite), with
470 occasional intraclasts of the same aphanotopic dolomite. Soft sediment deformation and
471 dolomicrite infill between mud clasts indicate that this sediment consisted of unlithified,
472 albeit cohesive, carbonate mud. Based on the abundance of fine mud, water energy was
473 probably not very high (Demicco and Hardie, 1994), although reworking and partial rounding
474 of the mud clasts requires at least occasionally higher water energies. According to the
475 standard microfacies concept, homogeneous aphanotopic dolomite falls into SMF 23 ("non-
476 laminated homogeneous micrite and microsparite without fossils"), indicating deposition in
477 "saline and evaporative environments, e.g. in tidal ponds" (Flügel, 2010). In addition, SMF 24
478 ("lithoclastic floatstones, rudstones and breccias") is observed in some of the beds where mud
479 clasts are abundant. These facies types are consistent with supersaturation-driven precipitation
480 of fine-grained authigenic carbonate in environments that were partially disconnected from
481 open seawater, and would match with a coastal sabkha environment and/or shallow ephemeral
482 lake. Ephemeral lakes may have formed on extended coastal alluvial plains along the Tethyan
483 margin during the Carnian, as suggested by Breda and Preto (2011). The fine mud may have
484 been homogenized and redistributed due to minor wave action in the ponds (cf. Ginsburg,
485 1971), which is often observed in ephemeral lake settings, explaining the formation of
486 homogeneous dolomite beds.

487 Episodic flooding of the alluvial plain by the dryland river system may have supplied water
488 to temporary evaporating ponds. Alternatively, the alluvial plain may have been sporadically
489 flooded by seawater, explaining the intercalations of authigenic dolomite layers with alluvial
490 clays (Breda and Preto, 2011). Homogeneous dolomites show a positive carbon isotope
491 signature between 0.7 and 4‰ VPDB (except one outlier), which is consistent with formation

492 from unaltered marine carbon in evaporative brine, with no significant contribution of ^{12}C
493 derived from organic matter. Evaporative conditions are also indicated by several gypsum
494 beds that occur between 45 and 70 m in the section, and pseudomorphs after gypsum, which
495 are observed in a thin section of a dolomite at 120 m (Fig. 4c, d). However, evaporites may
496 not always be preserved, as they are frequently dissolved due to seasonally wet conditions.
497 A bed of dolomitic ooid grainstone that is devoid of matrix occurs at 64 m (Fig. 4e), and
498 tempestites with moldic porosity indicative of dissolved allochems and dissolved fossils
499 occurs at several levels in the section, always associated to homogeneous dolomites. These
500 beds must represent events of higher water energy, contributing sediment from more open
501 marine areas. The presence of marine fossils, such as *Megalodon* bivalves, indicate that the
502 environment was influenced by marine conditions, at least episodically. The microfacies of
503 the oolite falls into SMF 15, which indicates proximity to the seaward edge of the platform.
504 Several beds containing abundant siliciclastic material (mainly angular quartz clasts) are
505 likely due to a riverine flooding event, which provided detrital material from the continent. In
506 general, the microfacies in the homogenous dolomite beds reflects both marine and
507 continental influences on the depositional environment.
508
509 *Laminated dolomite*
510 Laminated dolomites reminiscent of loferites (Fischer, 1964) occur in the upper part of the
511 clay-rich interval. The change from more homogeneous to laminated dolomite intercalations
512 correlates with the change from red to dark grey clay. The laminations consist of millimetre-
513 scale dolomite/clay interlayers, suggesting alternating deposition of clay and fine dolomite.
514 This microfacies falls into SMF 25 ("laminated evaporite-carbonate mudstone facies"),
515 indicating an "upper intertidal to supratidal sabkha facies in arid and semiarid coastal plains
516 and evaporitic lacustrine basins" (Flügel, 2010). Laminae showing soft sediment deformation
517 cannot be attributed to stromatolitic bindstone facies (SMF 19 to 21). Only some layers that

518 show a coarser fabric with interstitial dolosparite or dolomicrosparite containing putative
519 peloids have been interpreted as microbial laminites (Preto et al., 2015). Graded bedding
520 mostly indicates a direct sedimentation process rather than *in situ* precipitation of the primary
521 carbonate within a microbial mat (Vasconcelos et al., 2006; Bouton et al., 2016; Court et al.,
522 2017; Perri et al., 2018). A detrital origin of the clay in the dolomites is confirmed by a well-
523 ordered illite-smectite mixed-layer composition, which is atypical for authigenic clay
524 minerals. Frequent subaerial exposure and desiccation may explain why the sediment was not
525 homogenized and the lamination is preserved. This is supported by the occurrence of pseudo-
526 teepee structures as remnants of desiccation cracks. Rip-up clasts were formed during
527 subsequent flooding, when angular flat pebbles formed as the sediment was desiccated or
528 partially lithified. However, laminae commonly exhibit plastic deformation (e.g. in Fig. 3g)
529 where the mud was still unlithified.

530 Some uncertainty exists as to whether this facies was peritidal, or represents an ephemeral
531 lake, as suggested for the homogeneous dolomites above. Episodic high water-energy, as
532 indicated by the rip-up clasts, combined with frequent desiccation, could point to evaporative
533 tidal conditions that occur in a sabkha. What is atypical for a modern sabkha is the large
534 amount of clay input. This is attributed to seasonally wet conditions during the Carnian, and
535 the sediments can be considered to be a mixed facies of alluvial plain and coastal sabkha: a
536 "dirty" sabkha (see discussion below). Under such conditions, large amounts of evaporites, in
537 particular gypsum, could have been dissolved. Why the occurrence of laminated dolomites
538 coincides with the transition from red to grey clays is not clear, but may be related to more
539 permanently water-saturated conditions in the subsurface, while the surface was exposed to
540 periodic desiccation. These conditions would also be consistent with a sabkha environment.

541

542 *Nodular dolomite*

543 During intervals of arid conditions, the clay beds were subject to strong evaporation and
544 vadose diagenesis, causing oxidation and the red colour. Although red beds may also form in
545 humid environments if drainage is rapid (Sheldon, 2005), drainage was certainly slow due to
546 the large amounts of poorly permeable clay in the Travenanzes Fm., and the climate was
547 clearly seasonally arid (Breda and Preto, 2011). Dolomite nodules that occur sporadically
548 within certain intervals show internal brecciation, which must have occurred after
549 sedimentation. Internal brecciation is a typical feature of present day calcretes in arid
550 environments (e.g. Mather et al., 2018). Slightly negative $\delta^{13}C$-values indicate a contribution
551 of carbon derived from organic matter degradation, further suggesting that they formed within
552 the sediment. The formation of dolomite nodules could presumably be related to diagenesis in
553 palaeosols. In the upper part of the section (between 80 and 105 m) dolomite nodules are
554 associated with green reaction haloes along vertical peds in palaeosols of vertisol-calcisol
555 type (Preto et al., 2015). Carbonate formation may have been related to reducing fluids in
556 water-logged soils during humid intervals, while the cracks formed during desiccation in dry
557 periods, perhaps facilitated by the presence of expandable clay minerals (smectite).
558
559 **5.2 The origin of ionic solutions conducive to dolomite formation**
560 Overall, the dolomites in the Travenanzes Fm. show a facies association that matches a
561 variety of potential depositional environments. They have similarities to the Germanic Keuper
562 succession, and it is not entirely clear if a marine influence occurred, except where indicated
563 by marine fossils, as in the tempestite beds. Sr isotopes were analysed in order to better trace
564 the origins of ionic solutions to the environments that were conducive to dolomite formation.
565
566 *Strontium derived from seawater*
567 Radiogenic $^{87}Sr/^{86}Sr$ ratios can be indicative of the source of ionic solutions that the
568 dolomite precipitated from (Müller et al., 1990a; Müller et al., 1990b). Sr isotopes in selected

569 dolomites from the Travenanzes Fm. at the Dibona section show values between 0.707672
570 ±0.000003 and 0.707976 ±0.000004. Ammonoids found at the base of the succession suggest
571 a Tuvalian II age (*subbullatus* zone, 232.5-231.0 Ma; Ogg, 2012). The upper boundary of the
572 Travenanzes Fm. is time-transgressive, and hence the exact age is not known. We assume that
573 the sedimentation rate was at least as high, or higher, than in the peritidal carbonates of the
574 Dolomia Principale. In this region, the Dolomia Principale includes a part of the Rhaetian
575 (Neri et al., 2007) and, thus, its upper boundary is near the Triassic-Jurassic boundary at 201.3
576 Ma. Although the age interval of the Travenanzes Fm. is not precisely constrained, we
577 correlate the Dibona section (Fig. 11) with the Carnian seawater Sr-isotope curve (Korte et
578 al., 2003). The seawater curve was fixed at the lower boundary of the Travenanzes Fm. and
579 the time axis was varied to fit the seawater curve parallel to the envelope of minimal $^{87}Sr/^{86}Sr$
580 ratios measured in the dolomites (Fig. 11). The base of the first massive dolomite at 110 m in
581 the profile would therefore have an age of approximately 229 Ma.

582 Comparison with the seawater curve shows that the dolomites of the Travenanzes Fm. have
583 largely marine $^{87}Sr/^{86}Sr$ ratios (Fig. 11). Only values from micro-drilled samples extracted
584 with 0.1 N acetic acid were used for this reconstruction, and the resulting values all lie within
585 0.00022 of seawater values (grey shaded area). This scatter towards more positive values,
586 compared to seawater, may be due to a small influence by continental water. Indeed, during
587 deposition of the Travenanzes Fm. sufficient continental water would have been available
588 from rivers, and ions may have become concentrated while the water was evaporating in the
589 distal alluvial plain. Alternatively, Sr desorbed from clay minerals could have added more
590 radiogenic values to the brine. But even if a small influence of Sr of continental origin is
591 present, the marine signal is dominant because of the much higher Sr concentrations in
592 seawater.

593 The marine signature shown by the Sr isotopes does not support the classical Coorong
594 model for dolomite formation, where alkalinity is largely derived from continental

595 groundwater. The Coorong Lakes in South Australia are ephemeral lakes largely supplied by
596 groundwater (Von der Borch et al., 1975). Strangely, though, the $^{87}Sr/^{86}Sr$ ratios we measured
597 from Milne Lake (one of the Coorong Lakes) are similar to the ratio in modern seawater (Fig.
598 11), but this can be explained, as the local groundwater largely originates from a Pleistocene
599 carbonate aquifer, and accordingly, carry a Pleistocene Sr-isotope signature. A similar
600 scenario for the Travenanzes Fm. is unlikely as the only large-scale preceding carbonate
601 platforms at that time were the upper Ladinian-Carnian Cassian dolomite platforms (Russo et
602 al., 1997). Based on the stratigraphic context, all basins between these platforms were infilled
603 by the Heiligkreuz Fm. and an extremely flat topography was later established that is
604 stratigraphically overlain and sealed by the alluvial deposits of the laterally persistent
605 Travenanzes Formation. Furthermore, the Travenanzes Fm. consists of 100 m of impermeable
606 clay (including expandable clays), such that the long-distance transport of groundwater can be
607 excluded.

608 We conclude that the $^{87}Sr/^{86}Sr$ ratios of the dolomites represent a predominantly marine
609 influence. Presumably, seawater was transported to the interior of a coastal plain by episodic
610 flooding (spring tide or storm) events. Even in a seasonally wet climate, the contribution of Sr
611 from river water was insignificant compared to the influence of ions (including Sr) from
612 seawater that were concentrated by evaporation. Laminated dolomites in the uppermost part
613 of the section show values most similar to seawater composition, which is consistent with a
614 greater influence of peritidal conditions.

615

616 *The influence of Sr adsorbed to clay minerals*

617 Despite precautions to prevent contamination by other mineral phases by micro-drilling
618 and using mild reagents, some scatter occurs in the Sr-isotope data. Higher $^{87}Sr/^{86}Sr$ ratios in a
619 dolomite nodule may be due to a continental influence or perhaps more seasonally wet and
620 evaporative conditions with less of a marine influence. But higher values also may be due to

621 contamination and partial leaching of clay minerals within the dolomite samples. Within the
622 extraction sequence (1 M NaCl → 0.1 N acetic acid → 1 N acetic acid), the $^{87}Sr/^{86}Sr$ ratio
623 generally remains constant or becomes slightly less radiogenic, i.e., more similar to seawater.
624 However, the values strongly increase with leaching in 6 N HCl (Table 6). A modification of
625 $^{87}Sr/^{86}Sr$ ratios due to contamination by ^{87}Sr from the radioactive decay of ^{87}Rb to ^{87}Sr can be
626 considered as negligible since the concentrations of Rb was below the detection limit of 0.05
627 ppm (Table 5), and the half life is 48.8 billion years (Neumann and Huster, 1974). In addition,
628 the influence of celestine and Sr-rich barite, which were observed under SEM, on Sr-isotope
629 values can also be largely excluded. These mineral phases are bound to distinct layers of the
630 laminated dolomites, and they could be avoided by micro-drilling areas where the dolomite is
631 pure. Only one value from sample TZ14-9 shows extremely high Sr concentrations. This
632 sample was micro-drilled near a celestine layer, and it is therefore not surprising that a
633 celestine crystal may have been inadvertently sampled. The isotopic composition of the
634 celestine is also similar to Carnian seawater.

635 In the NaCl-fraction, only minimal amounts of dolomite are dissolved. The slightly more
636 radiogenic $^{87}Sr/^{86}Sr$ ratio may be derived from Sr that is lightly adsorbed to clay minerals and
637 finely dispersed in the clay matrix, although Sr^{2+} as a two-valent cation is more strongly
638 adsorbed to clay minerals than Na^{+}, and thus is not easily desorbed by NaCl. The values
639 approach seawater values in the 1 N acetic acid fraction with increasing extraction efficiency
640 and purity of the carbonate phase. Values from micro-drilled samples are also generally more
641 similar to seawater values, probably because more pure dolomite was sampled (PANGAEA
642 Data Archiving & Publication PDI-20535). 1 N acetic acid is usually observed to not strongly
643 attack interlayer ions in clay minerals.

644 Clay minerals leached in 6 N HCl show significantly more radiogenic values compared to
645 dolomite samples. This finding is consistent with strongly radiogenic values in the 6 N HCl-
646 fraction of dolomite samples (up to 0.730453 ±0.000005) and supports that the clay minerals

647 are the carriers of a Sr pool significantly more radiogenic than the carbonate phase showing
648 marine values. Sr is known to adsorb to illite-smectite mixed layer clay minerals (Missana et
649 al., 2008). The HCl-fraction most likely includes adsorbed Sr, and Sr occupying the interlayer
650 positions of the clay minerals, and presumably also structurally bound Sr in the clay mineral
651 phase. In particular, illite-smectite mixed-layer clay minerals, as detected by XRD of the clay
652 mineral separate in sample TZ14-9 (Fig. 7d), could have two different origins: burial
653 diagenesis and continental weathering. Based on the tectonic setting and shallow burial depth
654 of the Dolomites, the burial depth for smectite-illite transition has not been reached.
655 Therefore, these minerals are most likely derived from silicate weathering, with the Sr
656 signature representing the crustal origin of the parent rock. Our finding of radiogenic Sr-
657 isotope ratios supports that clay minerals did not incorporate Sr from seawater during a
658 sealevel stand. It is therefore clear that Sr extracted from the dolomites is not derived from
659 clay minerals.
660
661 *Dolomite as primary archive of Sr-isotope signatures*
662 The question is whether the Sr-isotope ratio reflects the conditions of dolomite formation
663 or whether it is inherited from a precursor phase. Baker and Burns (1985) and Vahrenkamp
664 and Swart (1990) documented very small distribution coefficients between aqueous and solid
665 solutions, and high Sr contents measured in Abu Dahbi sabkha dolomites (Müller et al.,
666 1990b) may be derived from precursor aragonite. However, if dolomite in the Travenanzes
667 Fm. is largely primary (Preto et al., 2015) and, thus, not formed from an aragonite precursor,
668 the Sr content should derive from the dolomite phase. Although some Sr may have been
669 released due to replacement of the dolomite, and excess Sr can explain the occurrence of
670 celestine and barite inclusions, nanocrystal structures imply that primary dolomite is partially
671 preserved. Indeed, Sánchez-Román et al. (2011) demonstrate a protodolomite forming in
672 culture experiments that contains Sr in the range of several thousand ppm. The incorporation

673 mechanism of Sr is still not entirely clear, since Sr is a large ion that should occupy the sites
674 of Ca in the crystal lattice. However, in Sánchez-Román et al. (2011), Sr appears to correlate
675 with the Mg content, and another incorporation mechanism may occur, such as surface
676 entrapment. Also the correlation of Sr contents with K contents could be explained by such a
677 mechanism of Sr incorporation. Even if only protodolomite formed in microbial culture
678 experiments (Gregg et al., 2015), natural modern dolomites are often rich in Sr (e.g. Meister
679 et al., 2007). The Sr could occur in disordered nano-structural domains that are not picked up
680 in the bulk XRD-signal. Non-classical nucleation and growth pathways, e.g. by nanoparticle
681 attachment, could play a role in the abnormal partitioning of Sr in the dolomite lattice. Thus, a
682 high Sr content in the Travenanzes Fm. or in Abu Dhabi Sabkha dolomites is likely a true
683 signature of primary dolomites.
684
685 **5.3 Mode of dolomite formation and comparison with known models**
686 *Primary dolomite formation*
687 Several results support a largely primary origin of dolomite in the Travenanzes Formation.
688 Formation temperatures reconstructed from oxygen isotopes (assuming Triassic seawater
689 composition of -1‰ VSMOW) are between 28 and 33°C. If a typical ^{18}O enrichment of 3‰
690 due to evaporation in a sabkha is assumed (McKenzie et al., 1980; McKenzie, 1981), the
691 calculated temperatures are between 40 and 50°C, which is still within the possible range in a
692 sakbha (cf. Hsü and Schneider, 1973). Both temperature and evaporation may have changed
693 over time, which may explain the observed linear trend in oxygen isotopes across the section
694 (Fig. 8B), although there is no co-variation between $\delta^{13}C$ and $\delta^{18}O$ as it would be expected
695 due to evaporation in hydrologically closed settings, such as the Germanic Keuper basin
696 (Reinhardt and Ricken, 2000; Arp et al., 2005). But also, the observed trend in $\delta^{18}O$ would be
697 too steep to be explained by overprinting within a normal geothermal gradient, and no signs
698 of any hydrothermal activity occur in this region. In any case, the oxygen isotope data do not

699 imply any post-depositional overprint, while nanocrystalline structures observed by Preto et
700 al. (2015) preclude a later pervasive recrystallization during burial diagenesis. Sedimentary
701 structures indicate that most of the homogenous dolomite and laminae containing aphanotopic
702 dolomite was unlithified, and dolomite was therefore deposited as fine-grained mud. This is
703 further supported by mm-scale interlayering of clay and dolomite in the laminated dolomites
704 near the top of the sequence, and some dolomite/clay couplets exhibiting fining-upward
705 bedding. Based on the observation of nanocrystal structures, replacement did not take place,
706 and it appears logical to assume that the primary phase was already dolomite.

707 While most of the dolomite may have been primary, micron-scale interstices between the
708 dolomicrite grains must have been cemented after deposition. This cementation resulted in
709 rims visible under SEM and result in near hexagonal compromise boundaries. The cement
710 may have contributed ^{13}C-depleted carbon during early diagenesis. The lowest $\delta^{13}C$ values of -
711 3.4‰ VPDB occur in the nodules. These nodules formed within the sediment, probably due
712 to reducing conditions and influenced by dissolved inorganic carbon from degrading organic
713 matter in the palaeosols. Homogeneous and laminated dolomites are clearly distinct from
714 nodules in their carbon isotope compositions (Fig. 8a), indicating only a minor contribution
715 from pore-water derived dissolved inorganic carbon. Carbon isotope values are thus largely
716 consistent with a primary precipitation. The mode of dolomite formation as fine mud and
717 subsequent cementation is comparable to several modern sites of dolomite formation.

718 While dolomite formation under Earth surface temperatures has been suggested to be
719 catalysed by microbes, perhaps by secreted organic polymers (EPS; cf. Bontognali et al.,
720 2013), this mechanism is currently under debate (cf. Gregg et al., 2015). The present study
721 does neither support nor rule out such a mechanism. We can raise the question whether
722 microbial EPS is enriched in the surface waters, where it may affect precipitation of fine
723 dolomite mud.

724

725 *The sabkha model*

726 The classical sabkha model involves dolomite formation under intra-supratidal conditions,
727 the concentration of brines through either seepage reflux (Adams and Rhodes, 1960) or
728 evaporative pumping (Hsü and Siegenthaler, 1969; Hsü and Schneider, 1973; McKenzie et
729 al., 1980; McKenzie, 1981), and precipitation of dolomite as Mg/Ca ratios increase due to
730 gypsum precipitation (see Machel, 2004, for a more detailed discussion of varieties of sabkha
731 models). This sabkha model allows for a mixture of seawater and continental groundwater,
732 with seawater mainly providing the ions for dolomite precipitation. Coastal sabkhas are
733 typically characterized by laminated (Lofer-type) dolomites, where the laminae are largely
734 unlithified after deposition (Illing, 1965; Bontognali et al., 2010; Court et al., 2017). In the
735 sabkha of Abu Dhabi, both pathways, via replacement of precursor aragonite and by direct
736 precipitation of dislocation-ridden primary dolomite, are observed (Wenk et al., 1993).

737 The sabkha model is thus a reasonable model for the uppermost parts of the Travenanzes
738 section, which contain laminated dolomites, marine Sr-isotope values and indications of
739 frequent desiccation and flooding in a peritidal setting. Yet, the conditions differed from the
740 modern sabkhas along the Persion Gulf due to the large amount of alluvial clay (dirty sabkha),
741 as opposed to aeolian sand. Most of the fine laminations may therefore result from
742 periodically varying conditions, perhaps with clay deposition during episodes of fluvial
743 discharge and carbonate deposition during evaporative conditions.

744

745 *The continental playa lake model*

746 The playa lake model was originally suggested by Eugster and Surdam (1973) for dolomite
747 of the Green River Formation (Wyoming), but the primary formation of fine dolomite mud is
748 observed in many alkaline playa lakes, such as Deep Springs Lake (Peterson et al., 1963;
749 Clayton et al., 1968; Meister et al., 2011), Lake Acigöl (Turkey; Balci et al., 2017), Lake
750 Neusiedl (Austria; cf. Neuhuber et al., 2016), and Lake Van (Turkey; McCormack et al.,

751 2018). For an overview see Eugster and Hardie (1978) and Last (1990). This type of setting
752 has also been suggested for the Germanic Keuper deposits during the late Carnian and Norian,
753 when the Germanic Basin was entirely disconnected from Panthalassa and was continental
754 (Reinhardt and Ricken, 2000). The Travenanzes Fm., with its homogeneous dolomite
755 intercalations in red and green clays, is strikingly similar to playa-lake Keuper facies in the
756 Germanic Basin. There, dolomite formed following evaporation and concentration of the
757 continental brines under a semi-arid climate.

758 Sr-isotope data, however, support a dominantly marine origin of ionic solutions to the
759 Travenanzes Fm., whereas Sr isotopes are strongly radiogenic in the Germanic Keuper
760 dolomites (or in Deep Springs Lake; Fig. 12). The two settings are thus fundamentally
761 different. Even dolomite nodules, showing somewhat more radiogenic values than seawater in
762 the Travenanzes Fm., still indicate a predominantly marine influence. The slightly more
763 radiogenic influence could be due to clay minerals present in the nodules that were difficult to
764 entirely separate from the carbonate. Also, dolomite nodules may have formed in relation to
765 palaeosols, during somewhat more humid times and, thus, may have been slightly influenced
766 by continental water input from rivers.

767

768 *The coastal ephemeral lake model (Coorong model)*

769 The Coorong model was proposed by Von der Borch et al. (1975), Von der Borch (1976),
770 Rosen et al. (1989) (see Warren, 2000, for detailed information) to explain the formation of
771 primary and uncemented dolomite in the Coorong lakes of South Australia. The Sr-isotope
772 values (Fig.12) show that the contribution of ionic solutions, and hence alkalinity, of
773 continental origin to the dolomitizing fluids was minimal, and that the dolomites are seawater
774 derived. This may be distinct from the typical Coorong model, where alkalinity is provided
775 from an inland karst system. But other coastal ephemeral lakes exist, including along the
776 Brasilian coast, north of Rio de Janeiro. Partially unlithified dolomite occurs in Brejo do

777 Espinho (Sánchez-Román et al., 2009), which is largely similar to the Coorong lakes, but
778 ionic solutions are mostly derived from seawater.

779 A coastal ephemeral lake model would probably be most suitable to explain homogeneous
780 dolomite beds of the Travenanzes Fm., where hypersaline ponds may have formed in a
781 dryland river system. However, unlike recent ephemeral lakes (such as Lagoa Vermelha,
782 Brejo do Espinho and the Coorong Lakes) the clay-rich sediment must have inhibited
783 groundwater flow. Hence, while modern coastal ephemeral lakes receive their water largely
784 through seawater percolating through porous dune sand, episodic flooding with seawater must
785 have provided ionic solutions for dolomite formation on a coastal plain.

786

787 *A system without modern analogue*

788 Overall, the depositional environment reconstructed for the Travenanzes Fm. shows
789 similarities to modern systems where dolomite forms. Among all the modern scenarios, a
790 coastal ephemeral lake model would be most similar to the conditions conducive to
791 homogeneous dolomites, lacking signs of frequent desiccation, while a coastal sabkha model
792 may explain the laminated intervals near the top of the studied succession. In contrast to
793 modern systems, the clay rich sediments of the Travenanzes Fm. preclude any input of
794 groundwater, which plays a role for ionic transport in both the modern day ephemeral lake
795 model and the different versions of sabkha models. Although modern systems provide valid
796 analogues for the mechanism of dolomite formation in the past, and probably throughout
797 Earth history, none of them is a faithful environmental analogue. The Carnian coastal plains
798 that covered an enormous area along the Tethys margin (Garzanti et al., 1995) represent a
799 system without a single modern analogue in terms of their sedimentary, hydrological and
800 climatic boundary conditions. In addition, the geochemistry of Tethys seawater may also have
801 been different from the modern seawater, an issue that requires further investigation (cf.
802 Burns et al., 2000; Li et al., 2018). These aspects need to be taken into account if we intend to

understand the conditions that led to dolomite formation through Earth history.

In the light of the possibility of spontaneous precipitation of fine dolomite mud in the water column, perhaps via formation and aggregation of nanoparticles, further discussion of a nucleation and growth pathway of dolomite is necessary. While several modifiers may also play a role in the water column, such as dissolved organic matter (Frisia et al., 2018), microbial EPS (Bontognali et al., 2013), or suspended clay particles (Liu et al., 2018), fluctuating conditions inducing spontaneous nucleation and growth of dolomite, in agreement with Ostwald's step rule (Deelman, 1999), require further consideration as a factor favourable for dolomite formation on a seasonally variable platform (Meister and Frisia, 2019).

The main finding of this study is that most of the dolomite in the >100 m thick Travenanzes Fm. probably formed through direct precipitation from a seawater-derived solution. This mode of primary dolomite formation has rarely been considered in the study of dolostone formations, but may explain the genesis of many other large-scale, fine-grained dolomite units that preserve fossils and sedimentary structures.

6 Conclusions

Dolomite beds intercalated in a 100-m-thick Carnian alluvial clay sequence in the Travenanzes Fm. largely formed as fine-grained primary mud. The depositional environment during times of dolomite formation most likely prevailed as ephemeral lakes in an extended coastal plain or dryland river system. The large amounts of clay are related to at least seasonally wet conditions; in addition, palaeosols and diagenetic dolomite nodules could have also formed under such conditions. The facies strongly resembles those of Triassic playa lakes found in the Germanic Basin, or in the modern Deep Springs Lake.

Sr isotopes clearly show a marine signature, indicating seawater as the main source of ions. The depositional environment is most similar to coastal ephemeral lakes resulting in the deposition of homogeneous dolomite beds through most of the sequence, changing into a

829 "dirty" sabkha near the top of the sequence, where fine dolomite/clay interlayers suggest
830 alternating deposition of extremely fine authigenic dolomite from evaporating water, and
831 clay.

832 Overall, Sr isotopes and petrographic observations provide insight into a system without
833 modern analogue, including elements of both coastal ephemeral lake systems and sabkhas as
834 the environment of primary dolomite formation. Considering the precipitation of primary
835 dolomite from coastal lakes or ponds may help explain other dolomite deposits with preserved
836 primary sedimentary features from throughout geologic history.

837

838

839 *Data availability*. All data mentioned in the text are in the article or available through the
840 Pangaea data repository.

841

842 *Author contributions*. Sampling: G. Arp, A. Breda, P. Meister, S. Klackl, N. Preto, M. Rieder;
843 Sr-isotope analysis: M. Horschinegg, M. Rieder, W. Wegner; C/O isotopes: S. Bernasconi;
844 XRD: S. Gier, M. Rieder, S. Klackl; petrography: P. Meister, M. Rieder, S. Klackl; concept
845 and idea of the study: P. Meister, N. Preto, U. Klötzli; writing the manuscript: P. Meister, M.
846 Rieder; proof-reading and correction: All authors; supervision: P. Meister

847

848 *Competing interests*. We declare no competing interests.

849

850 *Acknowledgements*. We thank C. Beybel, I. Wünsche, and L. Slawek for preparing high-
851 quality petrographic thin sections. Thanks also to W. Obermaier for analysing element
852 concentrations by ICP-OES and P. Körner for support during TOC measurements. S.
853 Niebergall provided some of the petrographic images. We furthermore thank S. Viehmann for
854 help during sampling and supervision of the students in the field and B. Bethke for her strong

855 support in the laboratory. Thanks also to M. Lorencak for the help during sampling of
856 dolomite from the Coorong Lagoon. We thank S. Frisia for input and constructive criticism.
857 We thank W. Blendinger, F. Franchi, S. Lokier, H. Machel, C. Romanek, an anonymous
858 reviewer, and the editor E. Samankassou for constructive comments. The study was partially
859 supported by the Marie Curie Intra-European Fellowship Project Triadol (Project no.
860 626025).

861

862 **References**

863 Adams, J.E., and Rhodes, M.L.: Dolomitization by seepage refluxion, Am. Assoc. Petrol.
864 Geol. Bull., 44, 1912–1921, DOI: 10.1306/0BDA6263-16BD-11D7-8645000102C1865D,
865 1960.
866 Alderman, A.R. and Skinner, H.C.W.: Dolomite sedimentation in the South-East of South
867 Australia, Am. J. Sci., 255, 561–567, DOI: 10.2475/ajs.255.8.561, 1957.
868 Arp, G., Hoffmann, V.-E., Seppelt, S., and Riegel, W.: Trias und Jura von Göttingen und
869 Umgebung, 74. Jahrestagung der Paläontologischen Gesellschaft, 2.-8.10.2004, Exkursion,
870 6, 147–192, Göttingen (Universitätsdrucke), http://dx.doi.org/10.23689/fidgeo-1790, 2004.
871 Arp, G., Bielert, F., Hoffmann, V.-E., and Löffler, T.: Palaeoenvironmental significance of
872 lacustrine stromatolites of the Arnstadt Formation ("Steinmergelkeuper", Upper Triassic,
873 N-Germany), Facies, 51, 419–441, https://doi.org/10.1007/s10347-005-0063-8, 2005.
874 Baker, P.A. and Burns, S.J.: Occurrence and formation of dolomite in organic-rich continental
875 margin sediments, Am. Assoc. Petrol. Geol. Bull., 69, 1917–1930, DOI:
876 10.1306/94885570-1704-11D7-8645000102C1865D, 1985.
877 Balci, N., Menekşe, M., Karagüler, N.G., Sönmez, M.S., and Meister, P.: Reproducing
878 authigenic carbonate precipitation in the hypersaline Lake Acıgöl (Turkey) with microbial
879 cultures, Geomicrobiology Journal, 33, 758-773,
880 https://doi.org/10.1080/01490451.2015.1099763, 2016.

881 Bontognali, T.R.R., Vasconcelos, C., Warthmann, R.J., Bernasconi, S.M., Dupraz, C.,
882 Strohmenger, C.J., and McKenzie, J.A.: Dolomite formation within microbial mats in the
883 coastal sabkha of Abu Dhabi (United Arab Emirates), Sedimentology, 57, 824–844,
884 https://doi.org/10.1111/j.1365-3091.2009.01121.x, 2010.
885 Bontognali T.R.R., McKenzie J.A., Warthmann R. and Vasconcelos C.: Microbially
886 influenced formation of Mg-calcite and Ca-dolomite in the presence of exopolymeric
887 substances produced by sulphate-reducing bacteria. Terra Nova, 26, 72–77,
888 https://doi.org/10.1111/ter.12072, 2013.
889 Bouton, A., Vennin, E., Pace, A., Bourillot, R., Dupraz, C., Thomazo, C., Brayard, A.,
890 Désaubliaux, G., and Visscher, P.T.: External controls on the distribution, fabrics and
891 mineralization of modern microbial mats in a coastal hypersaline lagoon, Cayo Coco
892 (Cuba), Sedimentology, 63, 972–1016, https://doi.org/10.1111/sed.12246, 2016.
893 Brack, P., Mundil, R., Oberli, F., Meier, M., and Rieber, H.: Biostratigraphic and radiometric
894 age data question the Milankovitch characteristics of the Latemar cycles (Southern Alps,
895 Italy), Geology, 24, 371–375, https://doi.org/10.1130/0091-
896 7613(1996)024<0371:BARADQ>2.3.CO;2, 1996.
897 Brack, P., Rieber, H., and Urlichs, M.: Pelagic successions in the Southern Alps and their
898 correlation with the Germanic Middle Triassic, Zentralbl. Geol. Paläontol. Teil I, 7–8,
899 853–876, http://hdl.handle.net/20.500.11850/158758, 1999.
900 Breitenbach, S.F.M. and Bernasconi, S.M.: Carbon and oxygen isotope analysis of small
901 carbonate samples (20 to 100 μg) with a GasBench II preparation device, Rapid Commun.
902 Mass Spectrom., 25, 1910–1914, https://doi.org/10.1002/rcm.5052, 2011.
903 Burns, S.J., McKenzie, J.A., and Vasconcelos, C.: Dolomite formation and biogeochemical
904 cycles in the Phanerozoic, Sedimentology, 47, 49–61, https://doi.org/10.1046/j.1365-
905 3091.2000.00004.x, 2000.

906 Breda, A. and Preto, N.: Anatomy of an Upper Triassic continental to marginal-marine
907 system: the mixed siliciclastic–carbonate Travenanzes Formation (Dolomites, Northern
908 Italy), Sedimentology, 58, 1613-1647, https://doi.org/10.1111/j.1365-3091.2011.01227.x,
909 2011.
910 Chilingar, G.V.: Relationship between Ca/Mg ratio and geological age, AAPG Bull., 40,
911 2256–2266, DOI: 10.1306/5CEAE577-16BB-11D7-8645000102C1865D, 1956.
912 Clayton, R.N., Jones, B.F., and Berner, R.A.: Isotope studies of dolomite formation under
913 sedimentary conditions, Geochim. Cosmochim. Acta, 32, 415–432,
914 https://doi.org/10.1016/0016-7037(68)90076-8, 1968.
915 Cleveland, D.M., Nordt, L.C., and Atchley, S.C.: Paleosols, trace fossils, and precipitation
916 estimates of the uppermost Triassic strata in northern New Mexico. Palaeogeography,
917 Palaeoclimatology, Palaeoecology, 257, 421–444,
918 https://doi.org/10.1016/j.palaeo.2007.09.023, 2008.
919 Court, W.M., Paul, A., and Lokier, S.W.: The preservation potential of environmentally
920 diagnostic sedimentary structures from a coastal sabkha, Marine Geology, 386, 1–18,
921 https://doi.org/10.1016/j.margeo.2017.02.003, 2017.
922 Czurda, K. and Nicklas, L.: Zur Mikrofazies und Mikrostratigraphie des Hauptdolomites und
923 des Plattenkalk-Niveaus der Klostertaler Alpen und des Rhätikon (Nördliche Kalkalpen,
924 Vorarlberg), In: Festband 300 Jahre Geol. Inst. Univ. Innsbruck, pp. 165–253, 1970.
925 Dal Corso, J., Mietto, P., Newton, R.J., Pancost, R.D., Preto, N., Roghi, G., and Wignall, P.B.
926 Discovery of a major negative $\delta^{13}C$ spike in the Carnian (Late Triassic) linked to the
927 eruption of Wrangellia flood basalts, Geology, 40, 79–82,
928 https://doi.org/10.1130/G32473.1, 2012.
929 Deelman, J.C.: Low-temperature nucleation of magnesite and dolomite, Neues Jahrbuch für
930 Mineralogie (Stuttgart), Monatshefte, 7, 289–302, 1999.

931 Demicco, R.V. and Hardie, L.A.: Sedimentary structures and early diagenetic features of
932 shallow marine carbonate deposits, SEPM Atlas, Ser., 1, 265,
933 https://doi.org/10.2110/sepmatl.01, 1994.
934 DePaolo, D.J. and Ingram, B.: High-resolution stratigraphy with strontium isotopes. Science,
935 227, 938–941, DOI: 10.1126/science.227.4689.938, 1985.
936 De Zanche, V., Gianolla, P., Mietto, P., Siorpaes, C., and Vail, P.R.: Triassic sequence
937 stratigraphy in the Dolomites (Italy), Sci. Geol. Mem., 45, 1–27, 1993.
938 Doglioni, C.: Tectonics of the Dolomites (Southern Alps-Northern Italy), J. Structural
939 Geology, 9, 181–193, https://doi.org/10.1016/0191-8141(87)90024-1, 1987.
940 Eugster, H.P. and Hardie, L.A.: Saline lakes, In: A. Lerman (Ed): Lakes, Chemistry, Geology,
941 Physics. Springer-Verlag, New York, N.Y., pp. 237-293, 1978.
942 Eugster, H.P. and Surdam, R.C.: Depositional environment of the Green River Formation of
943 Wyoming: a preliminary report, Bull. Geol. Soc. Am., 84, 1115-1120,
944 https://doi.org/10.1130/0016-7606(1973)84<1115:DEOTGR>2.0.CO;2, 1973.
945 Fischer, A.G.: The Lofer cyclothems of the Alpine Triassic, Kansas Geol. Surv. Bull. 169,
946 107–149, http://www.kgs.ku.edu/Publications/Bulletins/169/Fischer/index.html, 1964.
947 Flügel, E.: Microfacies of carbonate rocks - analysis, interpretation and application, 2nd.
948 Edition, Springer-Verlag Berlin Heidelberg, ISBN 978-3-642-03796-2, 2010.
949 Frisia, S.: Mechanisms of complete dolomitization in a carbonate shelf: comparison between
950 the Norian Dolomia Principale (Italy) and the Holocene of Abu Dhabi Sabkha, In: A
951 volume in honour of Dolomieu (Eds: B. Purser, M. Tucker, and D. Zenger), Spec. Publs.
952 Int. Ass. Sediment., 21, 55-74, https://doi.org/10.1002/9781444304077.ch5, 1994.
953 Frisia, S. and Wenk, H.-R.: TEM and AEM study of pervasive, multi-step dolomitization of
954 the upper Triassic Dolomia Principale (Northern Italy), J. Sed. Petrol., 63, 1049–1058,
955 https://doi.org/10.1306/D4267C94-2B26-11D7-8648000102C1865D, 1993.

956 Füchtbauer, H. and Goldschmidt, H.: Beziehungen zwischen Calzium-Gehalt und
957 Bildungsbedingungen der Dolomite, Geologische Rundschau, 55, 29–40, 1966.
958 Gattolin, G., Breda, A., and Preto, N.: Demise of Late Triassic carbonate platforms triggered
959 the onset of a tide-dominated depositional system in the Dolomites, Northern Italy,
960 Sedimentary Geology, 297, 38–49, https://doi.org/10.1016/j.sedgeo.2013.09.005, 2013.
961 Gattolin, G., Preto, N., Breda, A., Franceschi, M., Isottona, M., and Gianolla P.: Sequence
962 stratigraphy after the demise of a high-relief carbonate platform (Carnian of the
963 Dolomites): Sea-level and climate disentangled, Palaeogeogr., Palaeoclimatol., Palaeoecol.
964 423, 1–17, https://doi.org/10.1016/j.palaeo.2015.01.017, 2015.
965 Garzanti, E., Gnaccolini, M., and Jadoul, F.: Anatomy of a semiarid coastal system: the Upper
966 Carnian of Lombardy (Italy), Riv. Ital. Paleontol. Stratigr., 101, 17–36,
967 https://doi.org/10.13130/2039-4942/8563, 1995.
968 Gianolla, P., De Zanche, V., and Mietto, P.: Triassic sequence stratigraphy in the Southern
969 Alps (Northern Italy): definition of sequences and basin evolution, In: Mesozoic and
970 Cenozoic Sequence Stratigraphy of European Basins (Eds. deGraciansky P.-C., J.
971 Hardenbol, T. Jacquin and P.R. Vail), SEPM Spec. Publ., 60, 719–747,
972 https://doi.org/10.2110/pec.98.02.0719, 1998.
973 Ginsburg, R.N.: Landward movement of carbonate mud: new model for regressive cycles in
974 carbonates (abs.), AAPG Bull., 55, 340, 1971.
975 Given, R.K. and Wilkinson, B.H.: Dolomite abundance and stratigraphic age; constraints on
976 rates and mechanisms of Phanerozoic dolostone formation, J. Sediment. Research, 57,
977 1068–1078, https://doi.org/10.1306/212F8CF1-2B24-11D7-8648000102C1865D, 1987.
978 Gregg, J.M., Bish, D.L., Kaczmarek, S.E., and Machel, H.G.: Mineralogy, nucleation and
979 growth of dolomite in the laboratory and sedimentary environment: A review,
980 Sedimentology 62, 1749–1769, https://doi.org/10.1111/sed.12202, 2015.

981 Handy, M.R., Schmid, S.S., Bousquet, R., Kissling E., and Bernoulli, D.: Recoiling plate-
982 tectonic reconstructions of Alpine Tethys with the geological-geophysical record of
983 spreading and subduction in the Alps, Earth-Science Reviews 102, 121–158, DOI:
984 10.1016/j.earscirev.2010.06.002, 2010.
985 Hill, Jr., W.E., and Evans, D.R.: Solubility of twenty minerals in selected versene (EDTA)
986 solutions. State Geological Survey Kansas, Bull. 175, pp. 22,
987 http://www.kgs.ku.edu/Publications/Bulletins/175_3/index.html, 1965.
988 Hsü, K.J. and Siegenthaler, C.: Preliminary experiments on hydrodynamic movement induced
989 by evaporation and their bearing on the dolomite problem, Sedimentology, 12, 11–25,
990 https://doi.org/10.1111/j.1365-3091.1969.tb00161.x, 1969.
991 Hsü, K.J. and Schneider, J.: Progress report on dolomitization – hydrology of Abu Dhabi
992 Sabkhas, Arabian Gulf, The Persian Gulf. Springer, New York, pp. 409–422,
993 https://doi.org/10.1007/978-3-642-65545-6_20, 1973.
994 Iannace, A. and Frisia, S.: Changing dolomitization styles from Norian to Rhaetian in
995 southern Tethys realm, In: A Volume in Honour of Dolomieu (Eds. B. Purser, M. Tucker
996 and D. Zenger), Int. Assoc. Sedimentol. Spec. Publ., 21, 75–89,
997 https://doi.org/10.1002/9781444304077.ch6, 1994.
998 Illing, L.V., Wells, A.J. and Taylor, J.C.M.: Penecontemporary dolomite in the Persian Gulf,
999 In: Dolomitization and limestone diagenesis (Eds. L.C. Pray and L.C. Murray), SEPM
1000 Spec. Publ., 13, 89–111, https://doi.org/10.2110/pec.65.07.0089, 1965.
1001 Jones, B.F.: The hydrology and mineralogy of Deep Springs Lake, Inyo County, California,
1002 US Geol. Surv. Prof. Paper, 502-A, 56, https://doi.org/10.3133/pp502A, 1965.
1003 Korte, C., Kozur, H.W., Bruckschen, P., and Veizer, J.: Strontium isotope evolution of Late
1004 Permian and Triassic seawater, Geochim. Cosmochim. Acta 67, 47–62,
1005 https://doi.org/10.1016/S0016-7037(02)01035-9, 2003.

1006 Kraus, O.: Die Raibler Schichten des Drauzuges (Südliche Kalkalpen), Lithofazielle,
1007 sedimentpetrographische und paläogeographische Untersuchungen. Jb. Geol. B.-A., 112,
1008 81–152, 1969.
1009 Land, L.S.: Failure to precipitate dolomite at 25°C from dilute solution despite 1000-fold
1010 oversaturation after 32 years, Aquat. Geochem., 4, 361–368,
1011 https://doi.org/10.1023/A:1009688315854, 1998.
1012 Last, W.M.: Lacustrine dolomite – an overview of modern, Holocene, and Pleistocene
1013 occurrences, Earth-Science Reviews, 27, 221–263, https://doi.org/10.1016/0012-
1014 8252(90)90004-F, 1990.
1015 Li, M., Song, H., Algeo, T.J., Wignall, P.B., Dai, X., Woods, A.D.: A dolomitization event at
1016 the oceanic chemocline during the Permian-Triassic transition. Geology, 46, 1043–1046,
1017 https://doi.org/10.1130/G45479.1, 2018.
1018 Liu, D., Xu, Y., Papineau, D., Yub, N., Fan, Q., Qiu, X., and Wang, H.: Experimental
1019 evidence for abiotic formation of low-temperature proto-dolomite facilitated by clay
1020 minerals, Geochim. Cosmochim. Acta, 247, 83–95,
1021 https://doi.org/10.1016/j.gca.2018.12.036, 2019.
1022 Lumsden, D.N.: Discrepancy between thin-section and X-ray estimates of dolomite in
1023 limestone, J. Sed. Petrol., 49, 429–435, https://doi.org/10.1306/212F7761-2B24-11D7-
1024 8648000102C1865D, 1979.
1025 Machel, H.G.: Concepts and models of dolomitization: a critical reappraisal. Geological
1026 Society, London, Special Publications, 235, 7–63,
1027 https://doi.org/10.1144/GSL.SP.2004.235.01.02, 2004.
1028 Mather, C.C., Skrzypek, G., Dogramaci, S., and Grierson, P.F.: Paleoenvironmental and
1029 paleohydrochemical conditions of dolomite formation within a saline wetland in arid
1030 northwest Australia, Quaternary Science Reviews, 185, 172–188,
1031 https://doi.org/10.1016/j.quascirev.2018.02.007, 2018.

McArthur, J.M., Howarth, R.J., and Shield, G.A.: Strontium isotope stratigraphy. The geologic time scale, 2012, In: Gradstein, F.M., Ogg, J.G., Schmotz, M.D. and Ogg, G.M. (eds.), Elsevier, 1 of 2, 1144 pp, DOI: 10.1017/CBO9780511536045.008, 2012.

McCormack, J., Bontognali, T.R.R., Immenhauser, A., and Kwiecien, O.: Controls on cyclic formation of Quaternary early diagenetic dolomite, Geophysical Research Letters, 45, 3625–3634, https://doi.org/10.1002/2018GL077344, 2018.

McKenzie, J.: Holocene dolomitzation of calcium carbonate sediments from the coastal sabkhas of Abu Dhabi, U.A.E.. J. Geol., 89, 185–198, https://doi.org/10.1086/628579, 1981.

McKenzie, J., Hsü, K.J., and Schneider, J.F.: Movement of subsurface waters under the sabkha, Abu Dhabi, UAE and its relation to evaporative dolomite genesis. Spec. Publ.-SEPM, 28, 11–30, https://doi.org/10.2110/pec.80.28.0011, 1980.

Meister, P., Bernasconi, S., McKenzie, J.A., Vasconcelos, C., Frank, M., Gutjahr, M., and Schrag, D., Dolomite formation in the dynamic deep biosphere: Results from the Peru Margin (ODP Leg 201), Sedimentology, 54, 1007–1032, https://doi.org/10.1111/j.1365-3091.2007.00870.x, 2007.

Meister, P., Reyes, C., Beaumont, W., Rincon, M., Collins, L., Berelson, W., Stott, L., Corsetti, F., and Nealson, K.H.: Calcium- and magnesium-limited dolomite precipitation at Deep Springs Lake, California, Sedimentology, 58, 1810–1830, https://doi.org/10.1111/j.1365-3091.2011.01240.x, 2011.

Meister, P., McKenzie, J.A., Bernasconi, S.M., and Brack, P.: Dolomite formation in the shallow seas of the Alpine Triassic, Sedimentology, 60, 270–291, https://doi.org/10.1111/sed.12001, 2013.

Meister, P., Frisia, S.: Dolomite formation by nanocrystal aggregation in the Dolomia Principale of the Brenta Dolomites (northern Italy). Rivista Italiana di Stratigrafia e Paleontologia, 125, 183–196, https://doi.org/10.13130/2039-4942/11297, 2019.

1058 Missana, T., Garcia-Gutierrez, M., and Alonso, U.: Sorption of strontium onto illite/smectite
1059 mixed clays, Physics and Chemistry of the Earth, 33, 156–162,
1060 https://doi.org/10.1016/j.pce.2008.10.020, 2008.
1061 Moore, D.M. and Reynolds, R.C.: X-ray diffraction and the identification and analysis of clay
1062 minerals, Oxford University Press, New York, 378 p, ISBN: 0.19.505170.X, 1997.
1063 Müller, D.W., Mueller, P.A., and McKenzie, J.A.: Strontium isotopic ratios as fluid tracers in
1064 Messinian evaporites of the Tyrrhenian Sea (western Mediterranean Sea), In: Kastens,
1065 K.A., Mascle, J., et al., Proc. ODP, Sci. Results, 107: College Station, TX (Ocean Drilling
1066 Program), 603–614, DOI: 10.2973/odp.proc.sr.107.194.1990, 1990a.
1067 Müller, D.W., McKenzie, J.A., and Mueller, P.A.: Abu Dhabi sabkha, Persian Gulf, revisited:
1068 application of strontium isotopes to test an early dolomitization model, Geology, 18, 618–
1069 621, https://doi.org/10.1130/0091-7613(1990)018<0618:ADSPGR>2.3.CO;2, 1990b.
1070 Muttoni, G., Kent, D.V., Garzanti, E., Brack, P., Abrahamsen, N., and Gaetani, M.: Early
1071 Permian Pangea 'B' to Late Permian Pangea 'A', Earth Planet. Sci. Lett., 215, 379–394,
1072 https://doi.org/10.1016/S0012-821X(03)00452-7, 2003.
1073 Neri, C., Gianolla, P., Furlanis, S., Caputo, R., and Bosellini, A.: Note illustrative della Carta
1074 Geologica d'Italia alla scala 1:50.000, Foglio 029 Cortina d'Ampezzo, A.P.A.T. System
1075 Cart, Roma, 200 pp, 2007.
1076 Neuhuber, S., Steier, P., Gier, S., Draganits, E., and Kogelbauer, I.: Radiogenic Carbon
1077 Isotopes in Authigenic Carbonate from Lake Neusiedl, Austria, Geophysical Research
1078 Abstracts, 17, 15399–15399, 2015.
1079 Neumann, W., and Huster, E.: The half-life of ^{87}Rb measured as difference between the
1080 isotopes ^{87}Rb and ^{85}Rb. Zeitschrift für Physik, 270, 121–127, 1974.
1081 https://doi.org/10.1007/BF01677443

1082 Ogg, J.G.: Triassic, In: Gradstein, F. M., Ogg, J. G., Schmitz, M., and Ogg, G. (Eds.), The
1083 geologic time scale 2012, Elsevier, Cambridge University Press, Cambridge, 681–730,
1084 2012.
1085 Perri, E., Tucker, M.E., Słowakiewicz, M., Whitaker, F., Bowen, L., and Perrotta, I.D.:
1086 Carbonate and silicate biomineralization in a hypersaline microbial mat (Mesaieed sabkha,
1087 Qatar): Roles of bacteria, extracellular polymeric substances and viruses, Sedimentology,
1088 65, 1213–1245, https://doi.org/10.1111/sed.12419, 2018.
1089 Peterson, M.N.A., Bien, G.S., and Berner, R.A.: Radiocarbon studies of recent dolomite from
1090 Deep Springs Lake, California. J. Geophys. Res., 68, 6493–6505,
1091 https://doi.org/10.1029/JZ068i024p06493, 1963.
1092 Preto, N. and Hinnov, L.A.: Unravelling the origin of shallow-water cyclothems in the Upper
1093 Triassic Dürrenstein Formation (Dolomites, Italy). J. Sed. Res., 73, 774–789, DOI:
1094 10.1306/030503730774, 2003.
1095 Preto, N., Breda, A., Corso, J. D., Spötl, C., Zorzi, F., and Frisia, S.: Primary dolomite in the
1096 Late Triassic Travenanzes Formation, dolomites, Northern Italy: facies control and
1097 possible bacterial influence, Sedimentology, 62, 697–716,
1098 https://doi.org/10.1111/sed.12157, 2015.
1099 Randazzo, A.F. and Zachos, L.G.: Classification and description of dolomitic fabrics of rocks
1100 from the Floridan aquifer, U.S.A. Sediment. Geol., 37, 151–162,
1101 https://doi.org/10.1016/0037-0738(84)90005-8, 1983.
1102 Ratschbacher, L., Merle, O., Davy, P., and Cobbold, P.: Lateral extrusion in the Eastern Alps,
1103 Part 1: Boundary conditions and experiments scaled for gravity, Tectonics, 10, 245–256,
1104 https://doi.org/10.1029/90TC02622, 1991.
1105 Reinhardt, L. and Ricken, W.: The stratigraphic and geochemical record of Playa Cycles:
1106 monitoring a Pangaean monsoon-like system (Triassic, Middle Keuper, S. Germany),

1107 Palaeogeogr., Palaeoclimatol., Palaeoecol., 161, 205–227, https://doi.org/10.1016/S0031-
1108 0182(00)00124-3, 2000.
1109 Rieder, M., Wegner, W., Horschinegg, M., Preto, N., Breda, A., Gier, S., Klötzli, U.,
1110 Peckmann, J., and Meister, P. (2019) Strontium, carbon, and oxygen isotopes in Triassic
1111 dolomites - Travenanzes Formation (Italy). PANGAEA.
1112 https://doi.pangaea.de/10.1594/PANGAEA.902276
1113 Rodriguez-Blanco, J.D., Shaw, S., and Benning, L.G.: A route for the direct crystallization of
1114 dolomite, American Mineralogist, 100, 1172–1181, https://doi.org/10.2138/am-2015-4963,
1115 2015.
1116 Rosen, M.R., Miser, D.E., Starcher, M.A., and Warren, J.K.: Formation of dolomite in the
1117 Coorong region, South Australia, Geochim. Cosmochim. Acta, 53, 661–669,
1118 https://doi.org/10.1016/0016-7037(89)90009-4, 1989.
1119 Rosenbaum J. and Sheppard S.M.: An isotopic study of siderites, dolomites and ankerites at
1120 high temperatures, Geochim. Cosmochim. Acta 50, 1147–1150,
1121 https://doi.org/10.1016/0016-7037(86)90396-0, 1986.
1122 Russo, F., Neri, C., Mastandrea, A., and Baracca, A.: The mud mound nature of the Cassian
1123 Platform Margins of the Dolomites A case history: the Cipit boulders from Punta
1124 Grohmann (Sasso Piatto Massif, northern Italy), Facies, 36, 25–36,
1125 https://doi.org/10.1007/BF02536875, 1997.
1126 Sánchez-Román, M., Vasconcelos, C., Warthmann, R., Rivadeneyra, M.A., and McKenzie,
1127 J.A.: Microbial dolomite precipitation under aerobic conditions: results from Brejo do
1128 Espinho Lagoon (Brazil) and culture experiments, Int. Assoc. Sediment. Spec. Publ., 40,
1129 167–178, https://doi.org/10.1002/9781444312065.ch11, 2009.
1130 Sánchez-Román, M., McKenzie, J.A., Rebello Wagener, A., Romanek, C.S., Sánchez-Navas,
1131 A., and Vasconcelos, C.: Experimentally determined biomediated Sr partition coefficient

1132 for dolomite: Significance and implication for natural dolomite, Geochim. Cosmochim.
1133 Ac., 75, 887–904, https://doi.org/10.1016/j.gca.2010.11.015, 2011.
1134 Seegis, D.: Die Lehrbergschichten im Mittleren Keuper von Süddeutschland: Stratigraphie,
1135 Petrographie, Paläontologie, Genese, Hennecke, Remshalden, 382 pp, 1997.
1136 Sheldon, N.D.: Do red beds indicate paleoclimatic conditions?: A Permian case study.
1137 Palaeogeogr., Palaeoclimatol., Palaeoecol., 228, 305–319, 2005.
1138 Stampfli, G.M. and Borel, G.D.: A plate tectonic model for the Paleozoic and Mesozoic
1139 constrained by dynamic plate boundaries and restored synthetic oceanic isochrons, Earth
1140 Planet. Sci. Lett., 196, 17–33, https://doi.org/10.1016/S0012-821X(01)00588-X, 2002.
1141 Teal, C.S., Mazzullo, S.J., and Bischoff, W.D.: Dolomitization of Holocene shallow-marine
1142 deposits mediated by sulfate reduction and methanogenesis in normal-salinity seawater,
1143 northern Belize, J. Sediment. Research, 70, 649–663, https://doi.org/10.1306/2DC4092E-
1144 0E47-11D7-8643000102C1865D, 2000.
1145 Vahrenkamp, V.C. and Swart, P.K.: New distribution coefficient for the incorporation of
1146 strontium into dolomite and its implications for the formation of ancient dolomites,
1147 Geology, 18, 387–391, https://doi.org/10.1130/0091-
1148 7613(1990)018<0387:NDCFTI>2.3.CO;2, 1990.
1149 Van Tuyl, F.M.: The origin of dolomite, Annual Report 1914, Iowa Geological Survey, XXV,
1150 257–421, 1914.
1151 Vasconcelos, C., McKenzie, J.A., Warthmann, R., and Bernasconi, S.: Calibration of the $\delta^{18}O$
1152 paleo-thermometer with dolomite formed in microbial cultures and natural environments.
1153 Geology, 33, 317–320, DOI: 10.1130/G20992.1, 2005.
1154 Vasconcelos, C., Warthmann, R., McKenzie, J.A., Visscher, P.T., Bittermann, A.G., and van
1155 Lith, Y.: Lithifying microbial mats in Lagoa Vermelha, Brazil: Modern Precambrian
1156 relics? Sedimentary Geology, 185, 175–183, https://doi.org/10.1016/j.sedgeo.2005.12.022,
1157 2006.

1158 Veizer, J., Ala, D., Azmy, K., Bruckschen, P., Buhl, D., Bruhn, F., Carden, G.A.F., Diener,
1159 A., Ebneth, S., Godderis, Y., Jasper, T., Korte, C., Pawellek, F., Podlaha, O.G., and
1160 Strauss, H.: $^{87}Sr/^{86}Sr$, $\delta^{13}C$ and $\delta^{18}O$ evolution of Phanerozoic seawater, Chemical geology,
1161 161, 59–88, https://doi.org/10.1016/S0009-2541(99)00081-9, 1999.
1162 Von der Borch, C.C.: Stratigraphy and formation of Holocene dolomitic carbonate deposits of
1163 the Coorong area, South Australia, J. Sediment. Research, 46, 952–966,
1164 https://doi.org/10.1306/212F709F-2B24-11D7-8648000102C1865D, 1976.
1165 Von der Borch, C.C., Lock, D.E., and Schwebel, D.: Ground-water formation of dolomite in
1166 the Coorong region of South Australia, Geology, 3, 283–285, https://doi.org/10.1130/0091-
1167 7613(1975)3<283:GFODIT>2.0.CO;2, 1975.
1168 Warren, J.: Sedimentology and mineralogy of dolomitic Coorong Lakes, South Australia, J.
1169 Sedimentary Petrol., 60, 843–858, https://doi.org/10.1306/212F929B-2B24-11D7-
1170 8648000102C1865D, 1990.
1171 Warren, J.: Dolomite: occurrence, evolution and economically important associations, Earth-
1172 Science Reviews, 52, 1–81, https://doi.org/10.1016/S0012-8252(00)00022-2, 2000.
1173 Wenk, H.R., Meisheng, H., and Frisia, S.: Partially disordered dolomite: microstructural
1174 characterization of Abu Dhabi sabkha carbonates, Am. Mineral., 78, 769–774, 1993.
1175

1176 **Figure Captions**

1177 **Figure 1.** (**a**) Palaeogeographic map of Southern Alpine to Germanic domains during the
1178 middle Triassic; reproduced from Brack et al. (1999; modified). Bal: Balaton; BG: Burgundy
1179 Gate; Car: Carnian Alps; ECG: eastern Carpathian Gate; Lomb: Lombardy; NCA: Northern
1180 Calcareous Alps; SMG: Silesian Moravian Gate. The following cities are indicated for
1181 orientation: Mr: Marseille; Wa: Warsaw; Kr: Krakow; Be: Berlin; Fr: Frankfurt; Ly: Lyon.
1182 Inset: Tectonic map of the Southern Alps (Brack et al., 1996, modified) showing the sampling
1183 location at Rifugio Dibona. GL: Giudicarie Line; PL: Pustertal Line; VL: Val Sugana Line.

(**b**) Middle to Upper Triassic stratigraphy and distribution of facies within the Venetian Alps, showing a transition in geometries from a basin and platform topography during the lower Carnian to an extended alluvial to tidal plain in the upper Carnian. The shaded area indicates the Travenanzes Fm., showing a lateral transition in facies and a transgressive boundary with the Dolomia Principale. Compiled from Breda and Preto (2011), after De Zanche et al. (1993), modified.

Figure 2. Stratigraphic section at Rifugio Dibona: (**a**) Complete section modified after Breda and Preto (2011), showing sampling locations; (**b**) detailed section of the uppermost part of the clay-rich interval, showing sampling locations. (**c**) Outcrop photograph showing the uppermost grey part of the clay-rich interval including the location of the profile shown in (b).

Figure 3. Outcrop images of different types of dolomite intercalated with red and grey clay of the Travenanzes Fm. at Rifugio Dibona: (**a**) Homogeneous dolomite bed (15 cm thick; 33 m). (**b**) Upper part: dolomite nodules embedded in red clay, crosscut by green coloured cracks that are part of a calcic vertisol (95 m). (**c**) Laminated dolomite (110-112 m) interbedded with grey clay. (**d**) Bed containing gypsum nodules (Gy), along with gypsum-filled cracks at 50 m; (**e**) Dolomite-cemented conglomerate bed at 75 m. (**f**) Laminated bed showing soft sediment deformation (106 m); an isoclinal synsedimentary fold is indicated by the arrow. (**g**) Laminated dolomite showing folding of the laminae due to soft sediment deformation (same bed as in f).

Figure 4. Photomicrographs of thin sections of dolomites of the Travenanzes Fm.: (**a**) Rounded mud clasts embedded in dolomicrite matrix. The larger, mm-size intraclast in the upper left side of the image (arrow) consists itself of matrix with darker, embedded mud clasts (sample TZ16-St1; 104 m). (**b**) Mud clasts in dolomicrite matrix. Mud clasts are deformed

1210 (e.g., arrow); layers of coarser (C) and finer matrix (F) are equally affected by plastic
1211 deformation (sample TZ16-22; 120 m). (**c**, **d**) Pseudomorphs after gypsum in fine-grained
1212 dolomudstone (e.g., arrows). (**e**) Oolitic grainstone (sample TZ14-4; 64 m). The cortices
1213 consist of microcrystalline dolomite and lack a radial structure, some showing a concentric
1214 structure (arrow). (**f**) Laminated dolomite showing pseudo-teepee structures (arrow). Vertical
1215 cracks are often, but not always, associated with pseudo-teepees (sample TZ14-10; 107 m).
1216 Some coarser grained laminae may contain microsparite and peloids (P with small arrows).
1217 (**g**) Laminated dolomite showing both plastic and brittle deformation of laminae. A cm-scale
1218 pseudo-teepee occurs in the centre of the image (sample TZ 16-21; 107 m). (**h**, **i**) Closeup of
1219 graded lamina in (g) showing plastic deformation. The top of the lamina shows an erosion
1220 surface with small rip-up clasts (arrow), overlain by a coarser layer.
1221
1222 **Figure 5.** SEM images of dolomites in backscatter mode: (**a**) Overview showing a dolomite
1223 layer containing celestine inclusions (bright areas; Sample TZ14-9d; 95 m); (**b**) Celestine
1224 inclusion with barite in the centre (same sample as in a); (**c**) Barite crystals in dolomicrite
1225 (sample TZ14-4; 65 m).
1226
1227 **Figure 6.** SEM images of dolomites in backscatter mode showing different types of crystal
1228 shape: (**a**) Spheroidal growth of dolomite (darker areas) in clay layers (brighter areas; sample
1229 TZ14-9d; 95 m). (**b**) Closeup of a. (**c, d**) Dolomite crystals showing a porous interior and
1230 homogeneous syntaxial cement rims (c: sample TZ14-12; 90 m; d: sample TZ14-9d; 95 m).
1231
1232 **Figure 7.** X-ray diffraction patterns: (**a**) Bulk analyses of homogeneous dolomite (Samples
1233 TZ14-1, TZ14-7, and TZ14-9); main peaks and ordering peaks are labelled with (hkl) indices.
1234 The inset in (a) shows the Mg/(Ca+Mg) ratios in the dolomites determined from the shift of
1235 the 104 peak using the equation of Lumsden (1979) and the structural ordering calculated

1236 from the ratio of the 015 ordering peak to the 110 peak according to Füchtbauer and
1237 Goldschmidt (1966). (**b**-**d**) Clay mineral separates of samples TZ14-1, TZ14-7 and TZ14-9,
1238 air dried (N), saturated with ethylene glycol (EG), and heated to 550°C (T); d-values in Å.
1239 The illite-smectite mixed-layer is best seen in the ethylene-glycol saturated sample TZ14-9.
1240 The arrow points to the expandable (smectite) part of the mixed-layer.
1241
1242 **Figure 8.** (**a**) Carbon/oxygen isotope cross-plot shows a clear distinction between
1243 homogeneous, laminated, peloidal and nodular dolomites. Nodular dolomites are probably
1244 influenced by carbon derived from organic matter. (**b**) Oxygen isotope values ($\delta^{18}O$) show a
1245 positive trend with a gradient of 2‰ over the 100-m-thick stratigraphic section. This could be
1246 due to a decrease in precipitation temperature or to a change in the $\delta^{18}O$ of the water over
1247 time.
1248
1249 **Figure 9.** Element concentrations in sequentially extracted fractions of bulk dolomite and
1250 clay samples of the Travenanzes Fm.: (**a**) Ca plotted vs. Mg shows a linear trend, reflecting
1251 nearly the 1:1 stoichiometry of dolomite; (**b**) Sr shows some correlation with K, which could
1252 be due to incorporation in rapidly precipitating dolomite (see text for discussion).
1253
1254 **Figure 10.** Sr-isotope ratios and Sr concentrations measured in sequential and non-sequential
1255 extractions of dolomite and different control minerals. (**a-c**) Dolomite samples of the
1256 Travenanzes Fm. show consistently low Sr-isotope values (below 0.708000) in the 0.1 N
1257 acetic acid fraction and very high values in the HCl fraction. The values in the 1 N acetic acid
1258 fraction are higher in the micro-drilled samples, perhaps due to partial leaching of residual
1259 clay minerals. In bulk samples values are low, while concentrations indicate still abundant Sr,
1260 presumably from the dolomite phase. (**d**) Claystone samples show generally elevated Sr-
1261 isotope values (compared to the dolomite samples) and lower concentrations. Low Sr-isotope

values and higher concentrations in the acetic acid fractions of Sample TZ16-19B could be due to traces of carbonate in the sample. (**e, f**) Pure control materials, including barite, celestine, dolomite, and a mixture of these minerals show clear separation of the three fractions. Sr-isotope values in dolomites show some scattering, probably due to inhomogenities in the powder and the single crystals. The 2-sigma uncertainties are smaller than the symbol size.

Figure 11. Comparison of Sr isotopes in dolomites of the Travenanzes Fm. with the Carnian seawater curve (Korte et al., 2003) in grey. The 2-sigma uncertainties are smaller than the symbol size. Circled datapoints are clay samples or samples of nodules containing clay.

Figure 12. Sr-isotope values ($^{87}Sr/^{86}Sr$ ratios) in dolomites from different modern environments: Abu Dhabi Sabkha, Deep Springs Lake, Coorong Lakes; and from ancient environments: Germanic Keuper (Weser Fm. and Arnstadt Fm.); Travenanzes Fm. of the Dolomites, Southern Alps; in comparison with modern seawater (DePaolo and Ingram, 1985) and Triassic seawater (Korte et al., 2003).

ELECTRONIC SUPPLEMENT

Table S1. Petrographic summary including sedimentary structures from thin section analysis of dolomites from the Travenanzes Fm. at the Dibona section.

DATA IN REPOSITORY

PANGAEA Data Archiving & Publication:

https://doi.pangaea.de/10.1594/PANGAEA.902275

1287 **Table 1.** Compiled $^{87}Sr/^{86}Sr$ ratios of sequentially leached dolomites from different locations,
1288 clays and test minerals, using different extraction solutions.
1289
1290 **Table 2.** Elemental concentrations of leacheates from dolomites and clays used for Sr-isotope
1291 analysis.
1292
1293 **Table 3.** Total inorganic and organic carbon (TIC, TOC) contents of clay samples from the
1294 Travenanzes Formation.
1295
1296 **Table 4.** Carbon and oxygen isotope values of different types of dolomite from the
1297 Travenanzes Formation.
1298

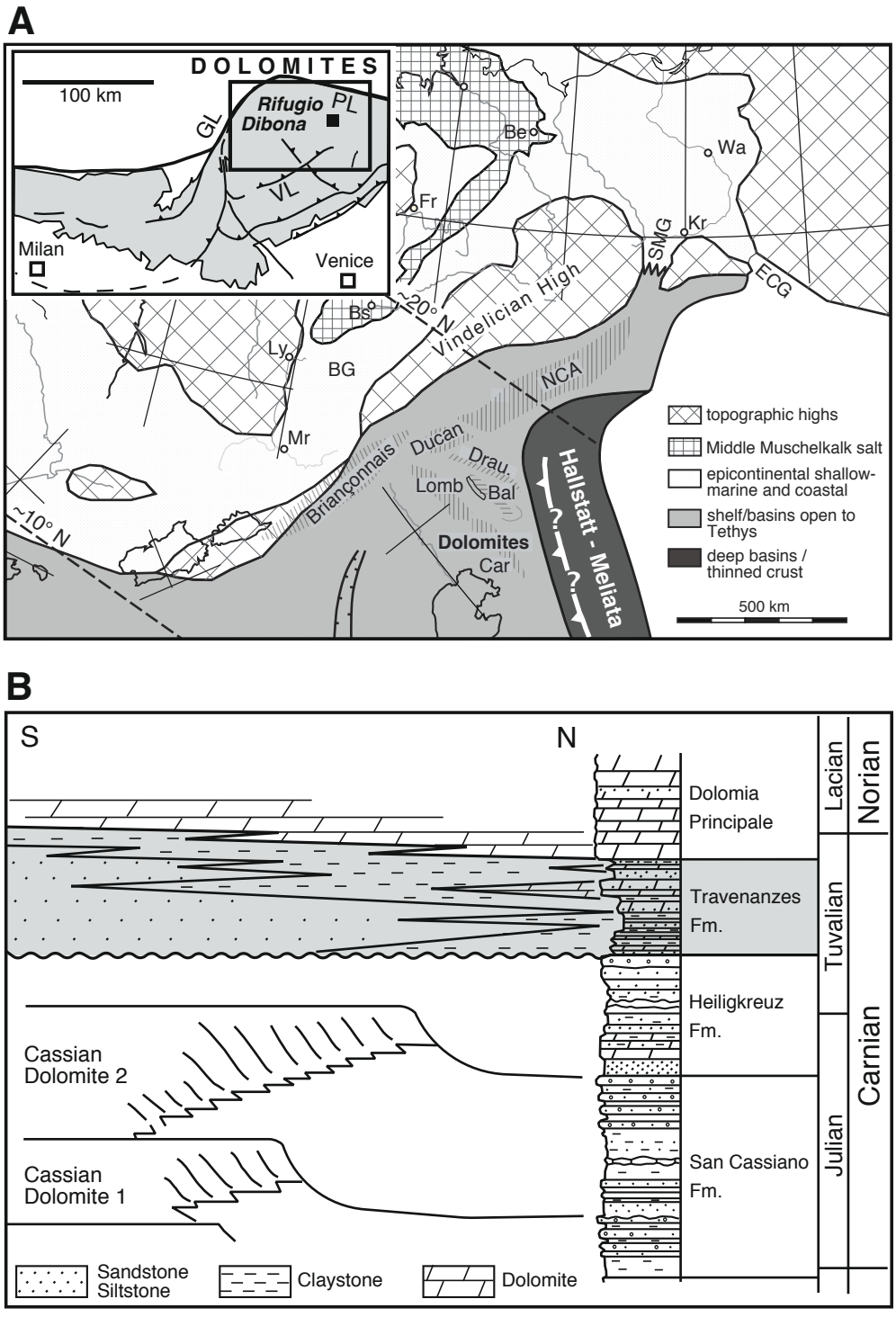
A
DOLOMITES
100 km
Rifugio Dibona
PL
GL
VL
Milan
Venice
Be
Wa
Fr
Kr
SMG
ECG
Bs
Ly
BG
20° N
Vindelician High
NCA
Mr
Ducan
Drau.
Briançonnais
Lomb
Bal
Hallstatt - Meliata
~10° N
Dolomites
Car
topographic highs
Middle Muschelkalk salt
epicontinental shallow-marine and coastal
shelf/basins open to Tethys
deep basins / thinned crust
500 km
B
S
N
Dolomia Principale
Travenanzes Fm.
Heiligkreuz Fm.
San Cassiano Fm.
Cassian Dolomite 2
Cassian Dolomite 1
Lacian
Norian
Tuvalian
Julian
Carnian
Sandstone Siltstone
Claystone
Dolomite

Figure 1

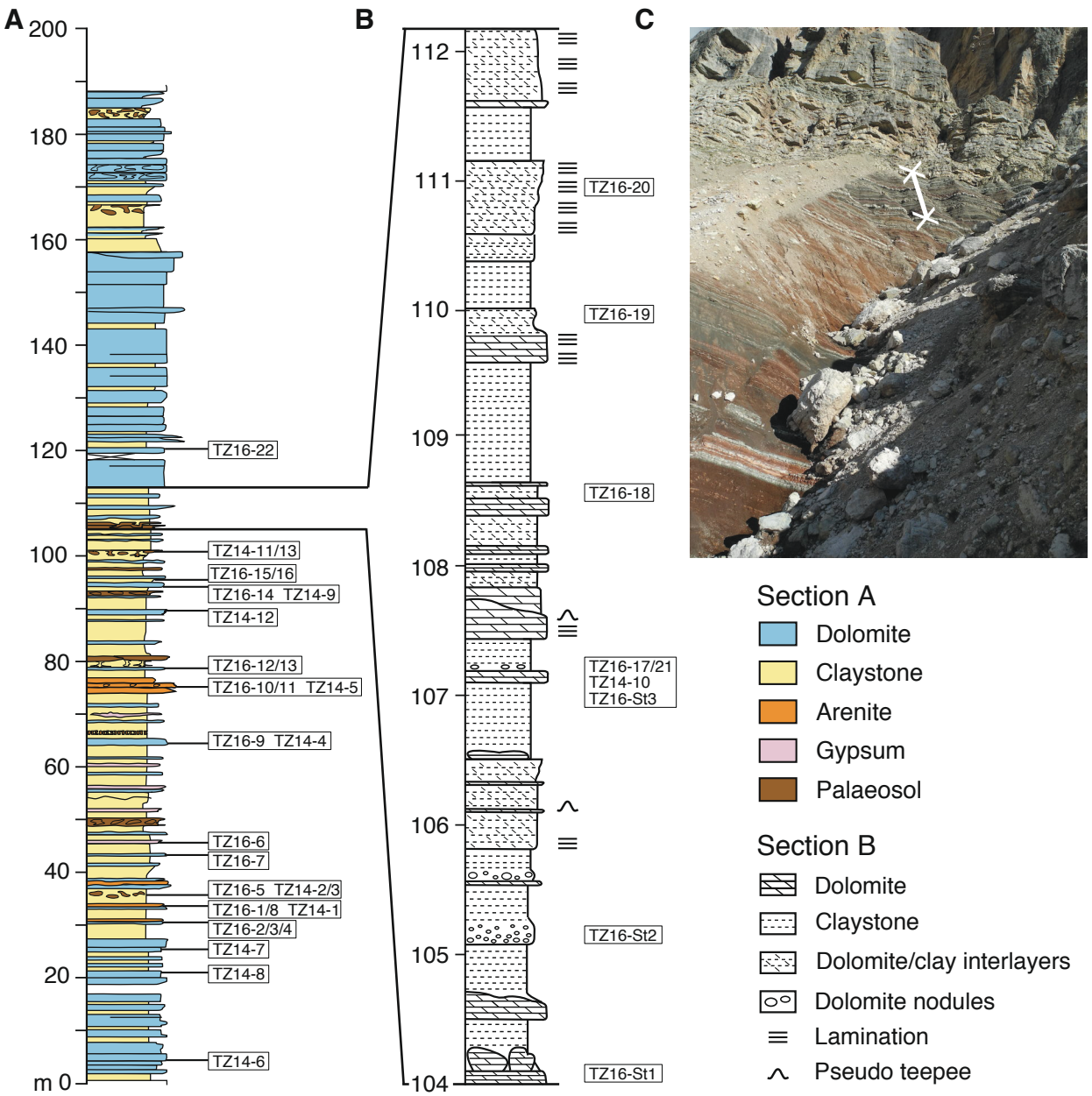
A
B
C
200
180
160
140
120
100
80
60
40
20
m 0
112
111
110
109
108
107
106
105
104
TZ16-22
TZ14-11/13
TZ16-15/16
TZ16-14 TZ14-9
TZ14-12
TZ16-12/13
TZ16-10/11 TZ14-5
TZ16-9 TZ14-4
TZ16-6
TZ16-7
TZ16-5 TZ14-2/3
TZ16-1/8 TZ14-1
TZ16-2/3/4
TZ14-7
TZ14-8
TZ14-6
TZ16-20
TZ16-19
TZ16-18
TZ16-17/21
TZ14-10
TZ16-St3
TZ16-St2
TZ16-St1
Section A
Dolomite
Claystone
Arenite
Gypsum
Palaeosol
Section B
Dolomite
Claystone
Dolomite/clay interlayers
Dolomite nodules
Lamination
Pseudo teepee

Figure 2

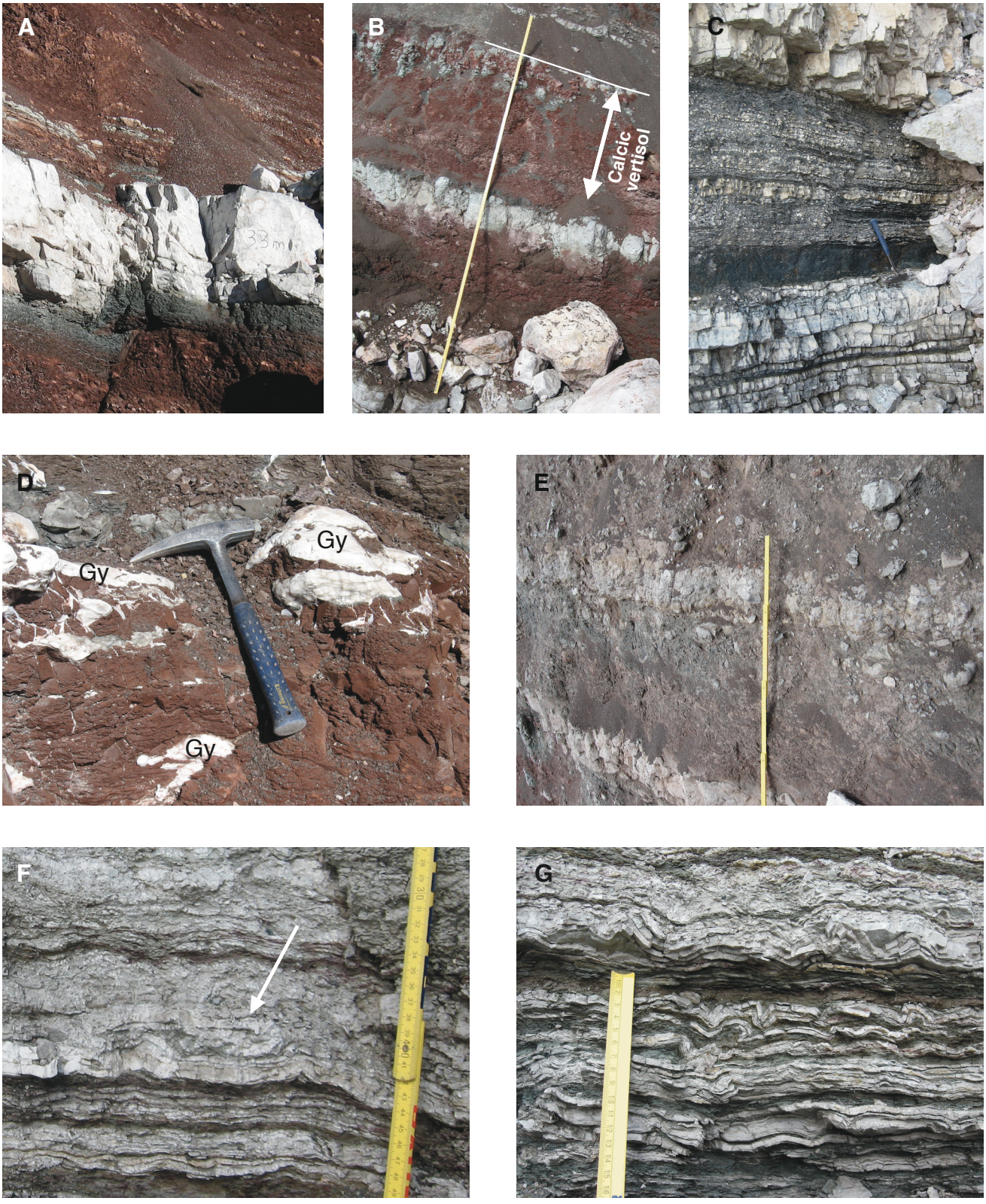

Figure 3

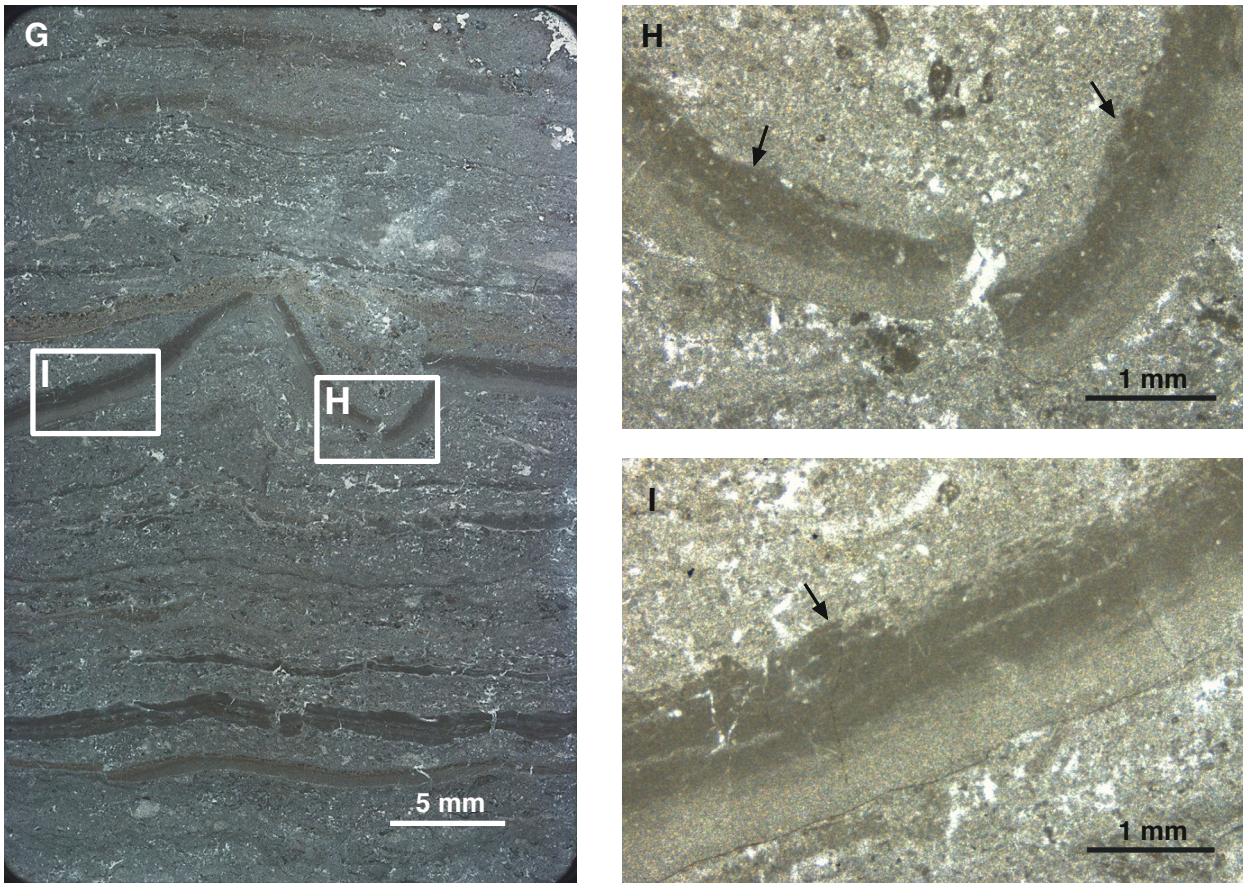

Figure 4 continued

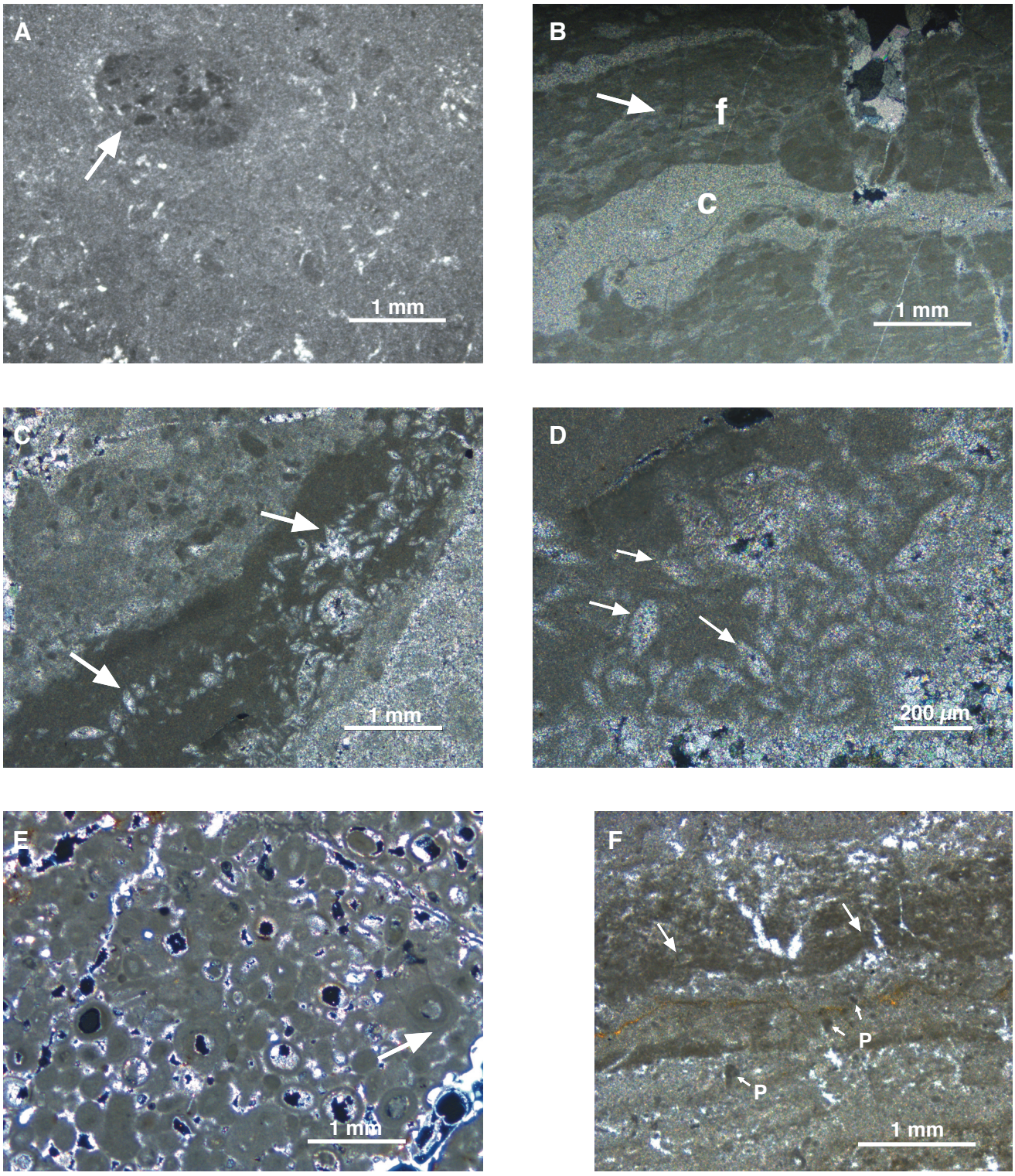

Figure 4

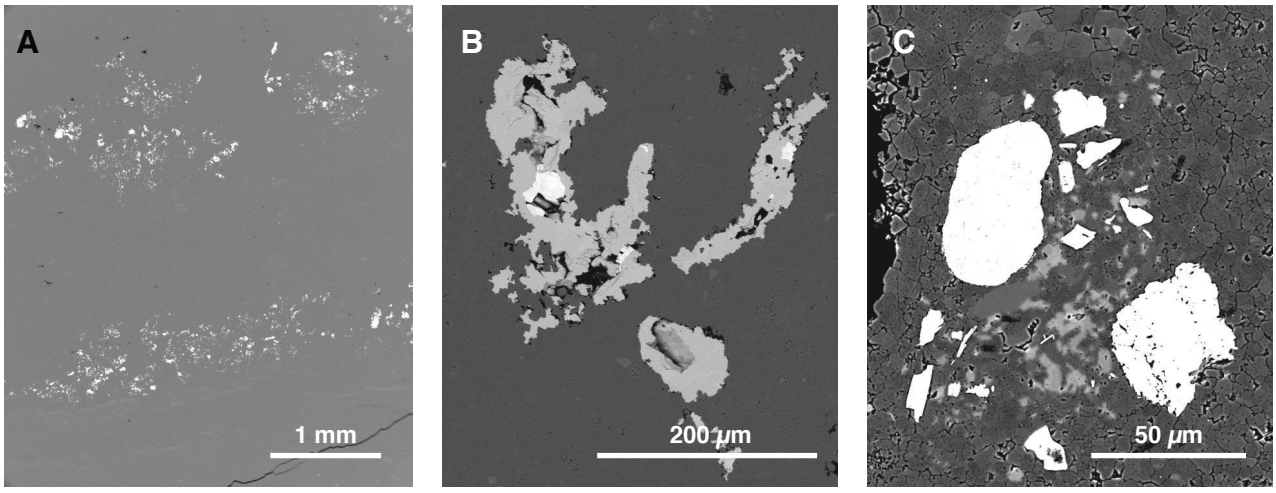

Figure 5

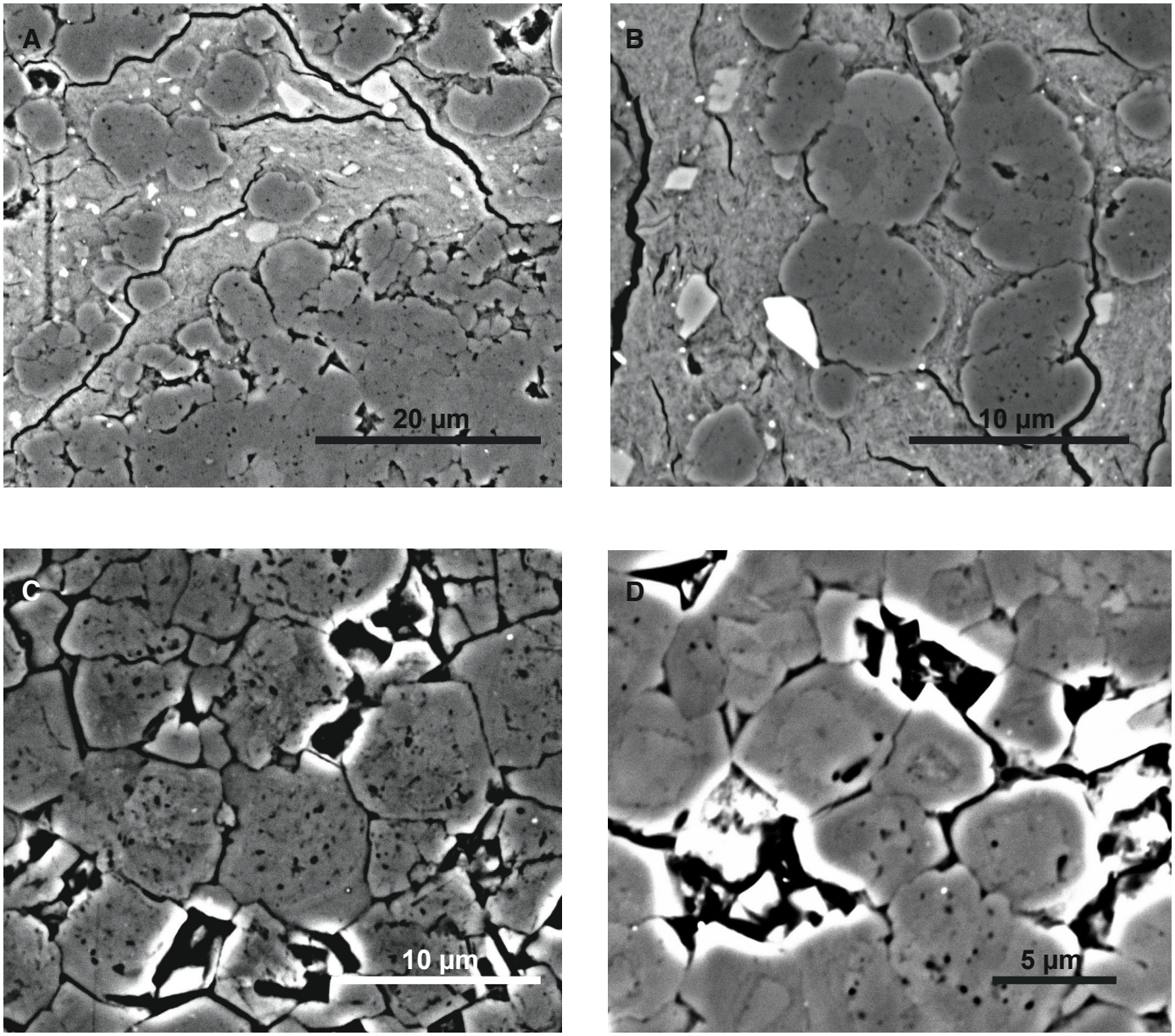

Figure 6

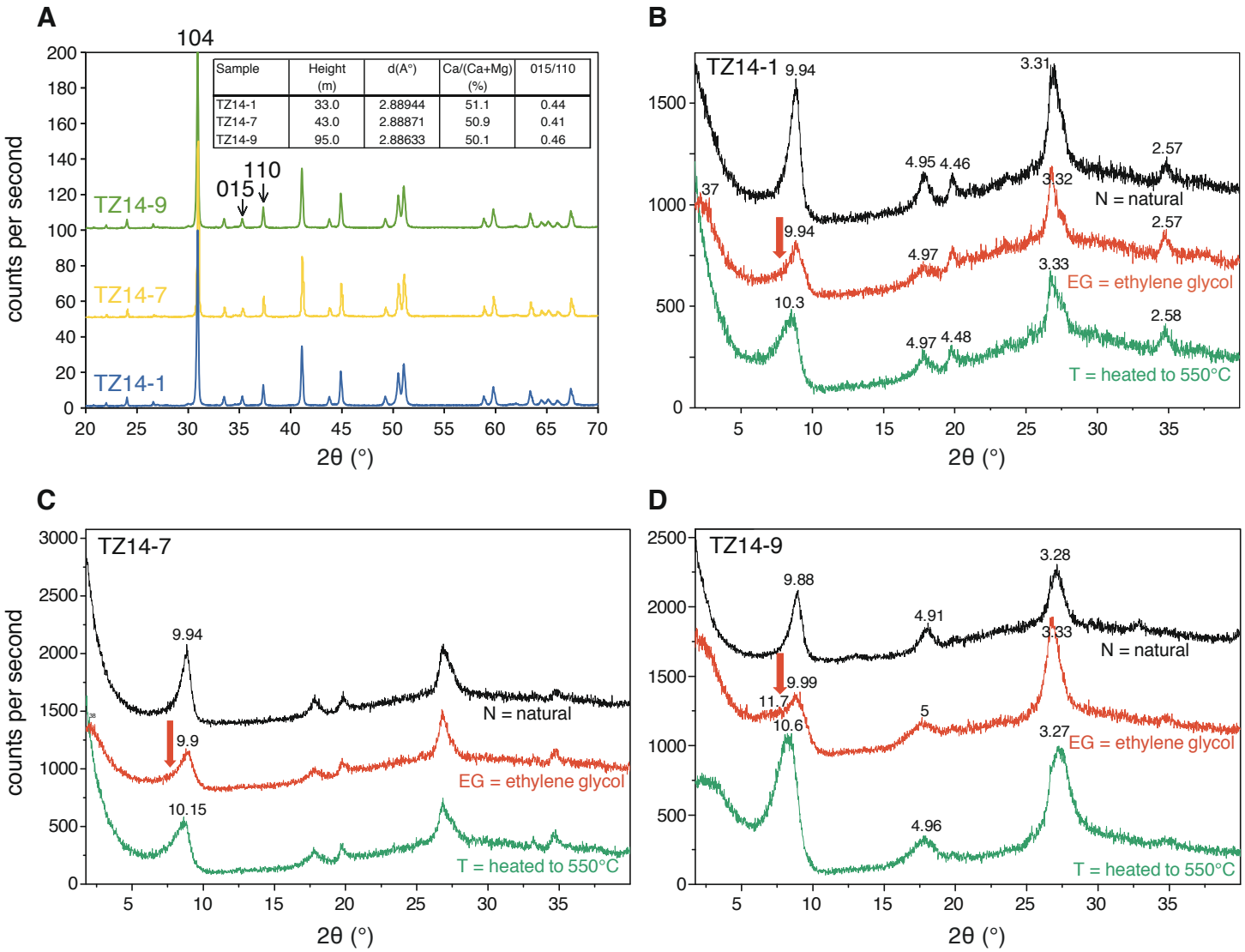
A
104
110
015
TZ14-9
TZ14-7
TZ14-1
counts per second
2θ (°)
Sample | Height (m) | d(A°) | Ca/(Ca+Mg) (%) | 015/110
TZ14-1 | 33.0 | 2.88944 | 51.1 | 0.44
TZ14-7 | 43.0 | 2.88871 | 50.9 | 0.41
TZ14-9 | 95.0 | 2.88633 | 50.1 | 0.46
B
TZ14-1
9.94
3.31
4.95
4.46
2.57
3.32
N = natural
9.94
4.97
2.57
3.33
EG = ethylene glycol
10.3
4.97
4.48
2.58
T = heated to 550°C
2θ (°)
C
TZ14-7
9.94
N = natural
9.9
EG = ethylene glycol
10.15
T = heated to 550°C
counts per second
2θ (°)
D
TZ14-9
9.88
3.28
4.91
3.33
N = natural
9.99
11.7
10.6
5
3.27
EG = ethylene glycol
4.96
T = heated to 550°C
2θ (°)

Figure 7

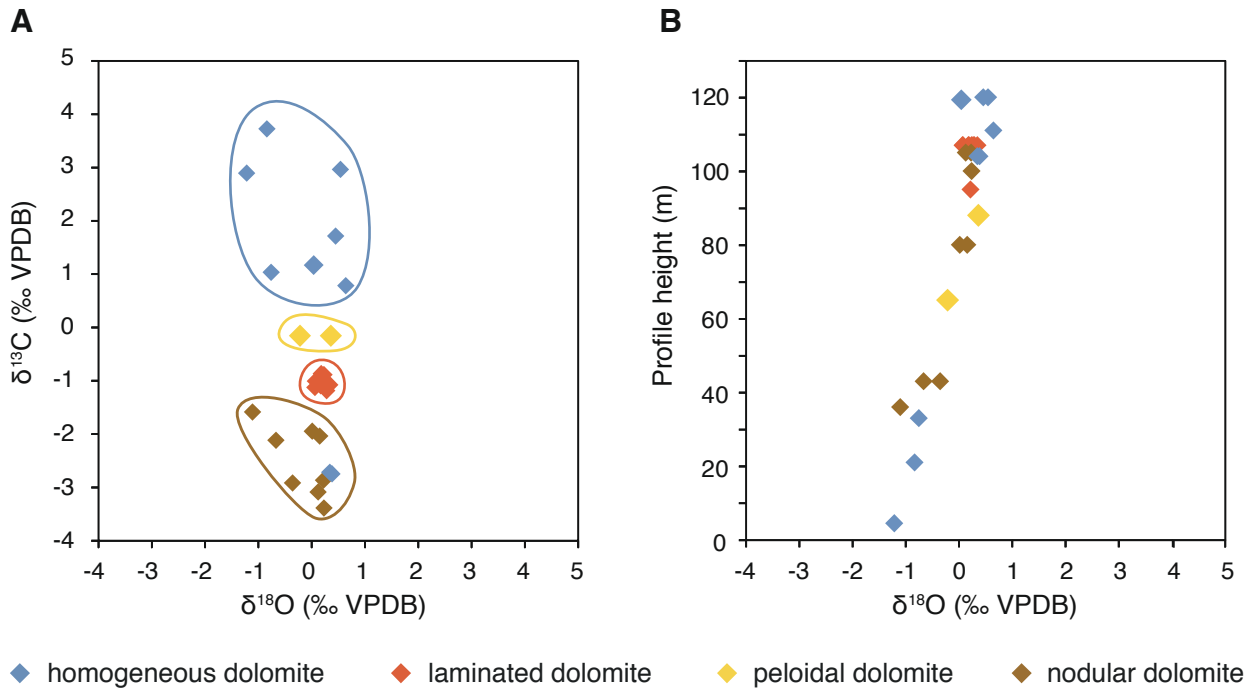
A
B
δ13C (‰ VPDB)
δ18O (‰ VPDB)
Profile height (m)
δ18O (‰ VPDB)
homogeneous dolomite
laminated dolomite
peloidal dolomite
nodular dolomite

Figure 8

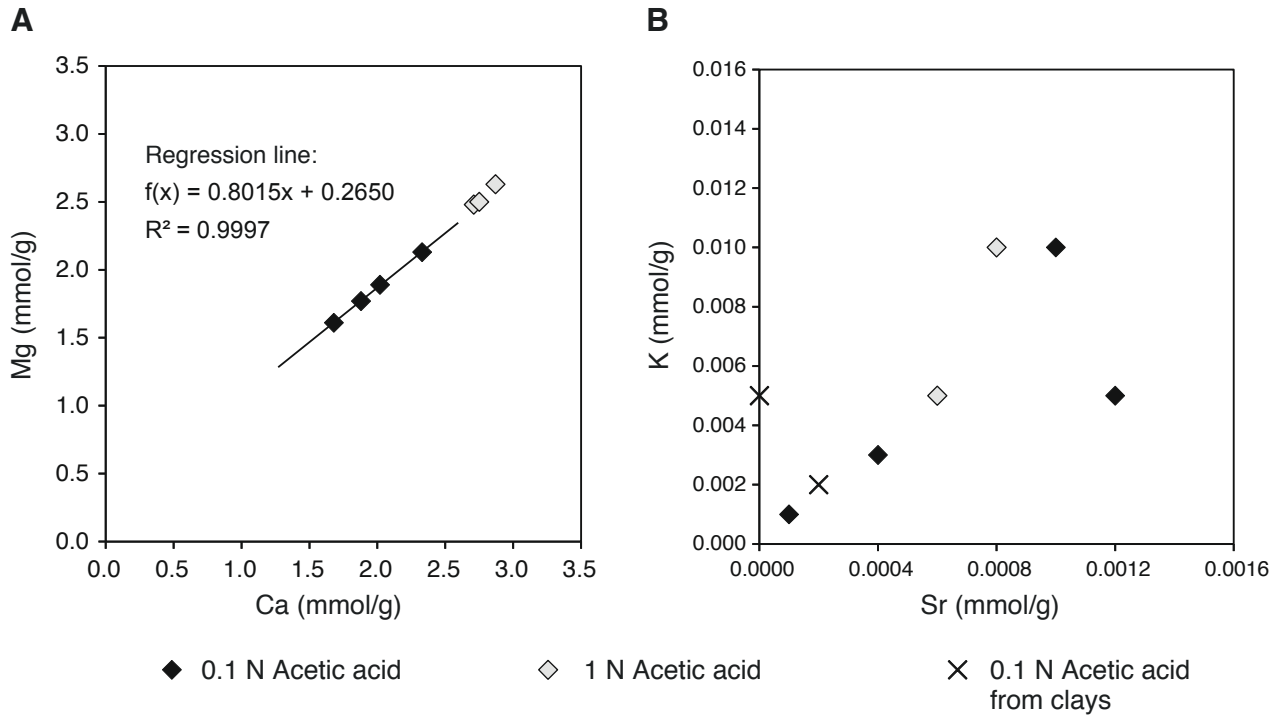
A
B
Regression line:
f(x) = 0.8015x + 0.2650
R² = 0.9997
Mg (mmol/g)
Ca (mmol/g)
K (mmol/g)
Sr (mmol/g)
0.1 N Acetic acid
1 N Acetic acid
0.1 N Acetic acid from clays

Figure 9

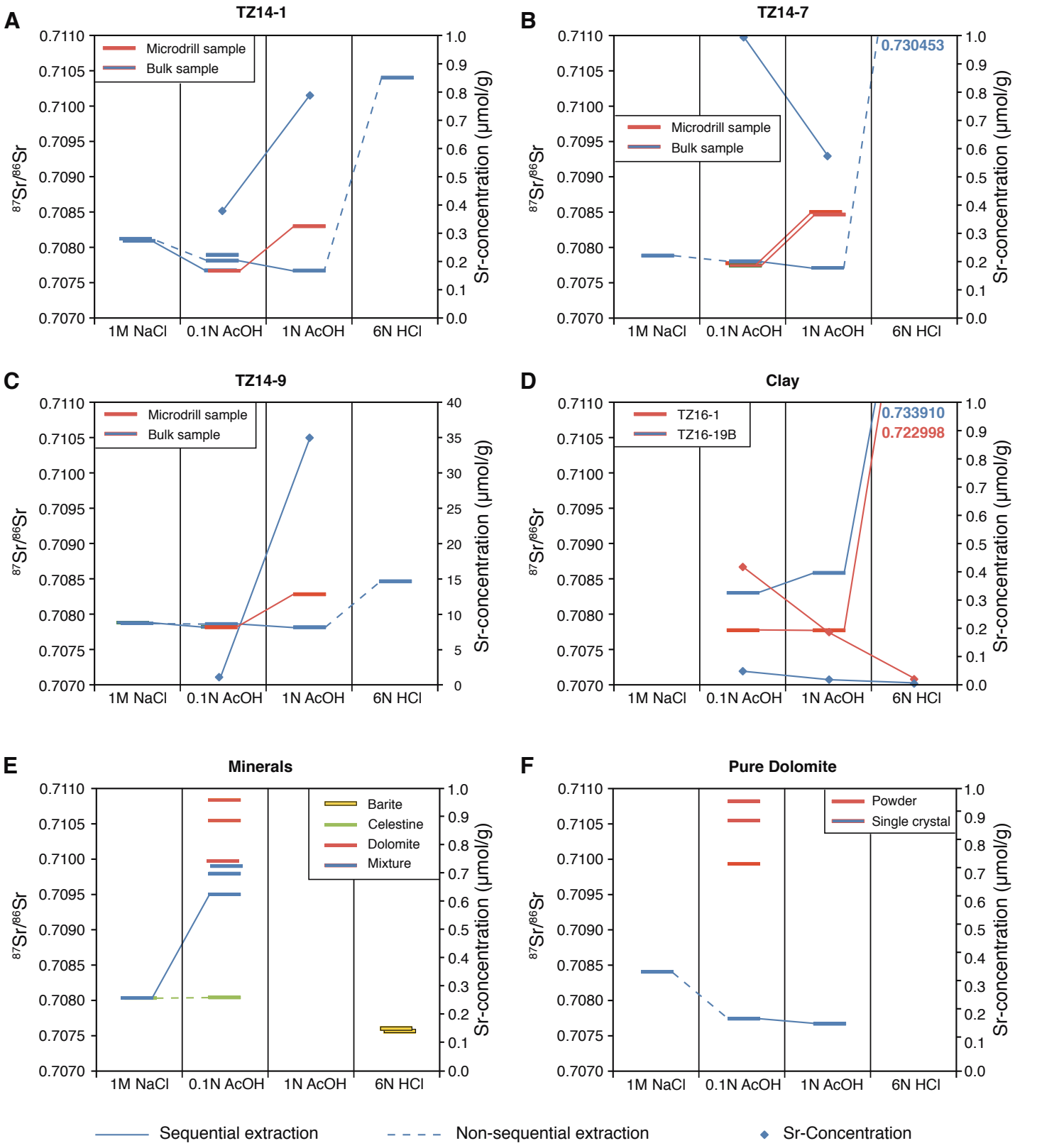
A
TZ14-1
Microdrill sample
Bulk sample
B
TZ14-7
0.730453
C
TZ14-9
D
Clay
TZ16-1
TZ16-19B
0.733910
0.722998
E
Minerals
Barite
Celestine
Dolomite
Mixture
F
Pure Dolomite
Powder
Single crystal
$^{87}Sr/^{86}Sr$
Sr-concentration (µmol/g)
1M NaCl
0.1N AcOH
1N AcOH
6N HCl
Sequential extraction
Non-sequential extraction
Sr-Concentration

Figure 10

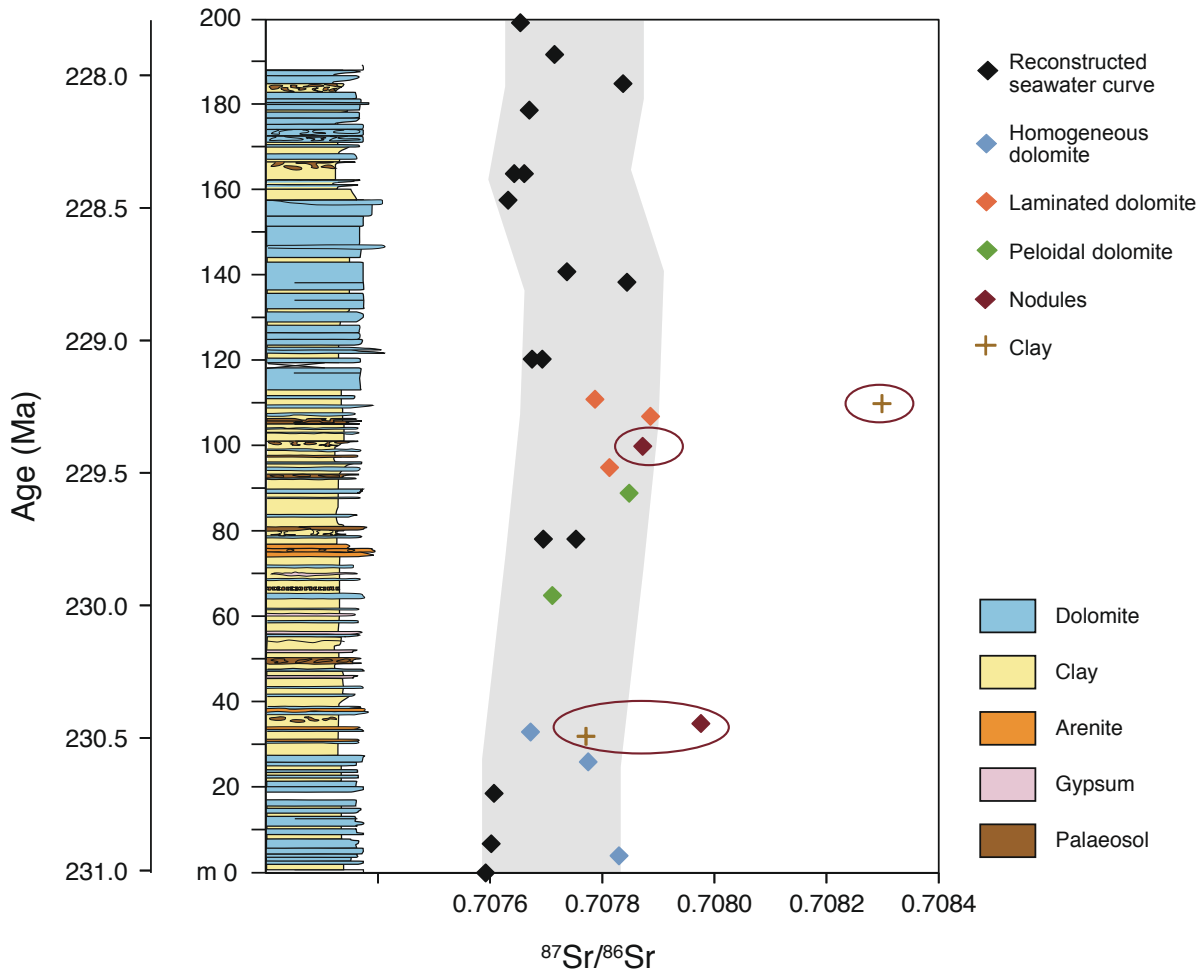
Age (Ma)
228.0
228.5
229.0
229.5
230.0
230.5
231.0
200
180
160
140
120
100
80
60
40
20
m 0
0.7076
0.7078
0.7080
0.7082
0.7084
87Sr/86Sr
Reconstructed seawater curve
Homogeneous dolomite
Laminated dolomite
Peloidal dolomite
Nodules
Clay
Dolomite
Clay
Arenite
Gypsum
Palaeosol

Figure 11

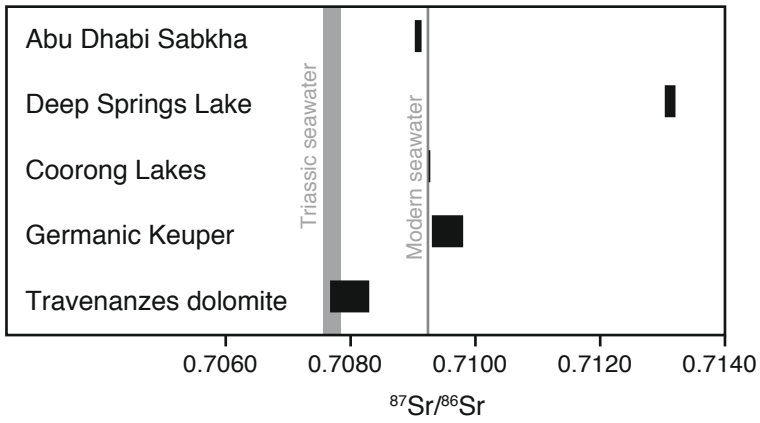
Abu Dhabi Sabkha
Deep Springs Lake
Coorong Lakes
Germanic Keuper
Travenanzes dolomite
Triassic seawater
Modern seawater
0.7060
0.7080
0.7100
0.7120
0.7140
87Sr/86Sr

Figure 12